

Dynamical stellar masses of pre-main sequence stars in Lupus and Taurus obtained with ALMA surveys in comparison with stellar evolutionary models

TERESA A. M. BRAUN,¹ HSI-WEI YEN,¹ PATRICK M. KOCH,¹ CARLO F. MANARA,² ANNA MIOTELLO,² AND LEONARDO TESTI^{2,3}

¹*Academia Sinica Institute of Astronomy and Astrophysics, 11F of Astro-Math Bldg, 1, Sec. 4, Roosevelt Rd, Taipei 10617, Taiwan*

²*European Southern Observatory (ESO), Karl-Schwarzschild-Str. 2, D-85748 Garching, Germany*

³*INAF/Osservatorio Astrofisico di Arcetri, Largo Enrico Fermi 5, I-50125 Florence, Italy*

ABSTRACT

We analysed archival molecular line data of pre-main sequence (PMS) stars in the Lupus and Taurus star-forming regions obtained with ALMA surveys with an integration time of a few minutes per source. We stacked the data of ¹³CO and C¹⁸O ($J = 2-1$ & $3-2$) and CN ($N = 3-2$, $J = 7/2-5/2$) lines to enhance the signal-to-noise ratios, and measured the stellar masses of 45 out of 67 PMS stars from the Keplerian rotation in their circumstellar disks. The measured dynamical stellar masses were compared to the stellar masses estimated from the spectroscopic measurements with seven different stellar evolutionary models. We found that the magnetic model of Feiden (2016) provides the best estimate of the stellar masses in the mass range of $0.6 M_{\odot} \leq M_{\star} \leq 1.3 M_{\odot}$ with a deviation of $<0.7\sigma$ from the dynamical masses, while all the other models underestimate the stellar masses in this mass range by 20% to 40%. In the mass range of $<0.6 M_{\odot}$, the stellar masses estimated with the magnetic model of Feiden (2016) have a larger deviation ($> 2\sigma$) from the dynamical masses, and other, non-magnetic stellar evolutionary models of Siess et al. (2000), Baraffe et al. (2015) and Feiden (2016) show better agreements with the dynamical masses with the deviations of 1.4σ to 1.6σ . Our results show the mass dependence of the accuracy of these stellar evolutionary models.

Keywords: Pre-main sequence stars (1290), Circumstellar disks (235), Stellar masses (1614), Stellar evolutionary models (2046)

1. INTRODUCTION

The mass is an important characteristic of a star. It determines not only the luminosity and temperature of the star, but also its evolution and feedback to the interstellar medium (Burkert 2004; Ceverino & Klypin 2009). Furthermore, mass determination of a large sample of young stars is essential to constrain the initial mass function (IMF). The IMF is a key to understand the physics of star formation and is also important to understand the evolution of stellar clusters and galaxies (Jeffries 2012; Hopkins 2018).

One method widely adopted to determine stellar masses uses the information of the luminosity and effective temperature of a star. By incorporating the physical processes acting on a star, theoretical models were established to describe the relationship between luminosity, effective temperature, mass and age of a star (e.g., D’Antona & Mazzitelli 1997; Baraffe et al. 1998; Palla & Stahler 1999; Siess et al. 2000; Bressan et al. 2012; Chen et al. 2014; Baraffe et al. 2015; Feiden 2016). The location of a star in the Hertzsprung Russel Diagram (HR

Diagram) is compared to the theoretical evolutionary tracks from the stellar evolutionary models to constrain the mass and age of the star. The advantage of this approach is the large number of stars that it can be applied to. With existing facilities it is possible to perform surveys on large samples of stars and provide data for the spectroscopic method to determine stellar masses (e.g., Rigliaco et al. 2012; Herczeg & Hillenbrand 2014; Alcalá et al. 2017; Manara et al. 2017).

The different stellar evolutionary models are in good agreement for main sequence (MS) stars and have been compared with various precise direct measurements of stellar mass (e.g., from orbital motion of binaries). Therefore, this method is considered reliable for MS stars (Hillenbrand & White 2004). However, the spectroscopic method has larger uncertainties for pre-main sequence (PMS) stars. The age and mass of a PMS star estimated with different models can show discrepancies of 10% to more than 50% (Sheehan et al. 2019). The theoretical models adopt different assumptions of convection, atmosphere, opacities and the equation of state

as well as different treatments of those processes, resulting in significant deviations in the estimated masses for PMS stars. Other influences, like magnetic fields, accretion, and dust in the atmosphere of a star, further complicate the models (Siess et al. 2000; Baraffe et al. 2009; Cassisi 2012; Baraffe et al. 2015). Therefore, further calibration of the stellar models of PMS stars is necessary.

One method to calibrate the stellar evolutionary models makes use of the orbital motions of eclipsing or resolved close binaries (e.g., Stassun et al. 2014; Rizzuto et al. 2016, 2019). By monitoring the motions of the stars, the stellar masses can be measured independently from the stellar evolutionary models. Because of the rareness of such binary systems and the time needed to closely monitor the orbital motions, the sample of stars which this method can be applied to is limited.

Another approach is to observe the rotation of protoplanetary disks around PMS stars (Sheehan et al. 2019; Simon et al. 2000, 2017, 2019). By measuring the velocity and radius of the material around a star by spectroscopic observations, it is possible to determine the enclosed mass with a minimum of assumptions. Different from the approach with binary systems, only one measurement is needed and the method is applicable to every star surrounded by a disk in Keplerian rotation. Hence, this can be used to obtain measurements of a large sample of PMS stars, suitable to test the theoretical models.

Dynamical mass measurements have been used in several surveys to test a number of different evolutionary models. Among these, there are smaller studies with three to nine stars (Simon et al. 2000; Sheehan et al. 2019), as well as larger studies, including 25 to 32 PMS stars (Hillenbrand & White 2004; Simon et al. 2017, 2019; Stassun et al. 2014). For PMS stars, it was found that the spectroscopic and dynamical masses are in good agreement for masses larger than about $1.2 M_{\odot}$ (Hillenbrand & White 2004; Stassun et al. 2014). Hillenbrand & White (2004) reported, that the evolutionary models examined in their paper tend to underestimate the stellar masses in the mass range below $1.2 M_{\odot}$. Whereas Stassun et al. (2014) found a tendency to overestimate stellar masses in this mass range by examining eclipsing binary systems. This tendency gets less significant when excluding the systems with tertiary components. The discrepancy in the results of Hillenbrand & White (2004) and Stassun et al. (2014) might be explained by the different stellar evolutionary models adopted because there are only two common models in these studies. Simon et al. (2019) updated several dynamical mass measurements with distances measured by Gaia (Gaia Collabo-

ration et al. 2016, 2018) and found an underestimation of stellar masses in the mass range of 0.4 to $1.4 M_{\odot}$ for evolutionary models which do not include magnetic fields (Baraffe et al. 2015; Feiden 2016). For the stellar evolutionary model of Feiden (2016) with magnetic fields, the discrepancy between dynamical and spectroscopic mass measurements becomes insignificant.

In order to further investigate the agreement of spectroscopic and dynamical mass measurements, wider mass ranges and different star-forming regions need to be examined. Especially the sample size of low mass stars ($< 0.5 M_{\odot}$) is so far limited. A larger sample of PMS stars is essential to verify the findings in previous studies.

With current facilities like ALMA it is possible to detect protoplanetary disks for large samples of stars in continuum emission at relatively high angular resolutions with short integration times of only a few minutes per source (e.g., Barenfeld et al. 2016; Ansdell et al. 2016, 2017; Ansdell et al. 2018; Long et al. 2018; Eisner et al. 2018; Cazzoletti et al. 2019; Williams et al. 2019; van Terwisga et al. 2020). In these observations, several molecular lines are often simultaneously observed. The obtained molecular-line data have lower signal-to-noise ratios (S/N) compared to the continuum data, which could be too low to constrain the velocity patterns in disks. However, by stacking data of different molecular lines and/or aligning line emission from different positions in a disk, it is possible to obtain sufficient signals and measure disk rotation and stellar mass (Yen et al. 2016; Matrà et al. 2017; Salinas et al. 2017; Teague et al. 2018b,a; Yen et al. 2018).

In this work, we aim to measure the masses of a large sample of PMS stars by making use of ALMA archival data obtained with shallow, but large surveys of nearby star-forming regions, and to compare the results to the spectroscopic masses determined with stellar evolutionary models. The structure of this paper is as follows: After introducing the sample and data in Section 2 and 3, the analysis is explained in Section 4. The results of the mass measurements are described in Section 5, followed by the discussion and comparison with stellar evolutionary models in Section 6. In the end the obtained insights are summarised, and future prospects are discussed in Section 7.

2. SAMPLE SELECTION

The sample of this study is selected from ALMA surveys at $0''.12 - 0''.25$ resolutions toward Young Stellar Objects (YSOs) in the young (~ 1 Myr to 3 Myr) and nearby (~ 150 pc to 160 pc) star-forming regions, Lupus and Taurus (Ansdell et al. 2016; Ansdell et al. 2018;

Long et al. 2019). The sample of the ALMA Lupus survey consists of 93 YSOs with spectroscopic masses of $M_* > 0.1 M_\odot$ and Class II or flat IR excess spectra located in the Lupus I, III and IV clouds (Ansdell et al. 2016; Ansdell et al. 2018). The sample of the ALMA Taurus survey consists of 42 YSOs of spectral types earlier than M3, excluding known, close binaries with separations of $0''.1-0''.5$ (Long et al. 2019). From these Lupus and Taurus samples, we selected those YSOs with resolved circumstellar disks in 1.3 mm continuum ALMA surveys, so that the inclination angles of the disks and their orientations on the plane of sky could be measured (Ansdell et al. 2018; Tazzari et al. 2017; Long et al. 2019; Manara et al. 2019). Thus, the sample in our study consists of 30 YSOs in the Lupus region and 37 YSOs in the Taurus region. The basic properties of our sample sources and the inclination angles and orientations of their circumstellar disks are listed in Table 1 and 2. The distribution of the effective temperatures and luminosities of the stars included in this paper are shown in Appendix A.

3. OBSERVATIONS

3.1. Lupus Region

For the YSOs located in the Lupus star forming region, we retrieved three data sets obtained with the Lupus survey from the ALMA archive, 2013.1.00220.S, 2015.1.00222.S (PI: J. Williams), and 2016.1.01239.S (PI: S. van Terwisga). The observations were conducted in Band 7 in Cycle 2 and in Band 6 in Cycle 3 with an integration time of approximately one minute per source. Additional observations to complete the sample were conducted in both Band 6 and 7 in Cycle 4 with an integration time of approximately four minutes per source. Apart from the continuum, several molecular lines were observed, including $^{13}\text{CO } J = 2-1$ and $3-2$ (220.399 GHz and 330.588 GHz), $\text{C}^{18}\text{O } J = 2-1$ and $3-2$ (219.560 GHz and 329.331 GHz) and the CN $N = 3-2$ transition. For the CN lines, we focus on the brightest hyperfine structure transitions of CN $J = 7/2-5/2$, with $F = 7/2-5/2$ and $F = 9/2-7/2$ at 340.247 770 GHz.

For the Band 7 observation in Cycle 2, 37 12-m antennas were used with baseline lengths from 21.4 m to 783.5 m. The native velocity resolution to observe the CO isotopologue and CN lines in Band 7 are 0.11 km s^{-1} and 0.31 km s^{-1} , respectively. 37 to 42 12-m antennas were used for the observation in Band 6 in Cycle 3 with baseline lengths from 15 m to 2483 m, and the CO isotopologue lines were observed at a native velocity resolution of 0.16 km s^{-1} . The observations in Cycle 4 were carried out with 44 12-m antennas and baseline lengths from 2600 m to 16 700 m in Band 6 and 41 12-m an-

tennas and baseline lengths from 1100 m to 15 100 m in Band 7. The native velocity resolutions in Cycle 4 are 0.11 km s^{-1} and 0.17 km s^{-1} for the CO isotopologue lines in Band 7 and Band 6, respectively, and 0.22 km s^{-1} for CN. Further details of the observations are described in Ansdell et al. (2016); Ansdell et al. (2018) and van Terwisga et al. (2018).

3.2. Taurus Region

For the YSOs located in the Taurus star forming region, we retrieved the data set obtained with the project 2016.1.01164.S (PI: G. Herczeg) from the ALMA archive. The observations were conducted in Band 6 in Cycle 4 with an integration time of approximately four minutes per source for bright sources and ten minutes per source for the other sources. The observations were carried out using 45 to 47 12-m antennas with baselines of 21 m to 3697 m. In addition to the 1.3 mm continuum emission, ^{13}CO and $\text{C}^{18}\text{O } J = 2-1$ were observed at a native velocity resolution of 0.16 km s^{-1} . Further information about the observations can be found in Long et al. (2018, 2019).

3.3. Data Reduction and Imaging

After obtaining the raw visibility data from the ALMA archive, the data were calibrated with the pipeline of the Common Astronomy Software Applications package CASA. Each data set was calibrated with the CASA version recommended by the ALMA observatory. For the Lupus sample the following CASA versions were used: 2013.1.00220.S with CASA 4.2.2, 2015.1.00222.S with CASA 5.1.1 and 2016.1.01239.S with CASA 4.7.2. The data of the Taurus sample were partly calibrated with CASA 4.7.2 and CASA 5.1.1. More information about the calibration of the Taurus data is given in Long et al. (2018, 2019).

We extracted the molecular lines by subtracting the continuum emission from the calibrated visibility in the uv-plane. The ranges of line-free velocity channels were inspected manually. Afterwards the images were generated from the visibility data and cleaned using the task `clean` in CASA, with `briggs` weighting with a robust parameter of +0.5. The channel widths of 0.17 km s^{-1} and 0.12 km s^{-1} were adopted to generate images of the CO isotopologue $J = 2-1$ and $3-2$ lines, respectively. Because of the coarse native spectral resolution of the CN data, the channel width of 0.22 km s^{-1} was adopted to generate CN images. For further analysis, all the images for a given source were convolved to the coarsest resolution among them using the CASA task `imsmooth` and regridded to have the same spatial axes. In addition, the intensity of the $J = 3-2$ emission is higher than

Table 1. Parameters adopted from the literature for the analysis for stars in the Lupus region

Name	RA	Dec	i	PA	dist	T_{eff}	L_{\star}	Ref.
			[$^{\circ}$]	[$^{\circ}$]	[pc]	[K]	[L_{\odot}]	
Sz65	15:39:27.75	-34:46:17.56	61.46 \pm 0.88	108.63 \pm 0.37	155	4060	0.89	1
J15450887-3417333	15:45:08.85	-34:17:33.81	36.30 \pm 5.56	2.41 \pm 2.53	155	3060	0.06	1
Sz68	15:45:12.84	-34:17:30.98	32.89 \pm 3.32	175.78 \pm 3.13	154	4900	5.42	1
Sz69	15:45:17.39	-34:18:28.66	43.53 \pm 8.65	124.28 \pm 17.10	155	3197	0.09	1
Sz71	15:46:44.71	-34:30:36.05	40.82 \pm 0.71	37.51 \pm 0.01	156	3632	0.33	1
Sz73	15:47:56.92	-35:14:35.15	49.76 \pm 3.95	94.71 \pm 5.17	157	4060	0.46	1
Sz75	15:49:12.09	-35:39:05.46	60.2 \pm 5.0	169.0 \pm 5.0	152	4205	1.48	2
Sz76	15:49:30.72	-35:49:51.83	-60.0 \pm 5.0	65.0 \pm 5.0	160	3270	0.18	2
RXJ1556.1-3655	15:56:02.08	-36:55:28.67	53.5 \pm 5.0	55.6 \pm 5.0	158	3705	0.26	2
Sz83	15:56:42.29	-37:49:15.82	3.31 \pm 2.90	163.76 \pm 5.94	160	4060	1.49	1
Sz84	15:58:02.50	-37:36:03.08	73.99 \pm 1.56	167.31 \pm 0.77	153	3125	0.13	1
Sz129	15:59:16.45	-41:57:10.66	31.74 \pm 0.75	154.94 \pm 0.43	162	4060	0.43	1
RYLup	15:59:28.37	-40:21:51.56	68.0 \pm 5.0	109.0 \pm 5.0	159	4900	1.87	2
J16000236-4222145	16:00:02.34	-42:22:14.99	65.71 \pm 0.36	160.45 \pm 0.02	164	3270	0.18	1
MYLup	16:00:44.50	-41:55:31.27	72.98 \pm 0.35	58.94 \pm 0.12	157	5100	0.85	1
EXLup	16:03:05.48	-40:18:25.83	-30.5 \pm 5.0	70.0 \pm 5.0	158	3850	0.76	2
Sz133	16:03:29.37	-41:40:02.14	78.53 \pm 0.65	126.29 \pm 0.09	153	4350	0.07	1
Sz90	16:07:10.05	-39:11:03.64	61.31 \pm 5.34	123.00 \pm 4.86	160	4060	0.42	1
Sz98	16:08:22.48	-39:04:46.81	47.10 \pm 0.70	111.58 \pm 0.06	156	4060	1.53	1
Sz100	16:08:25.75	-39:06:01.60	45.11 \pm 0.97	60.20 \pm 0.06	137	3057	0.08	1
J16083070-3828268	16:08:30.69	-38:28:27.28	74.0 \pm 5.0	107.0 \pm 5.0	156	4900	1.84	2
SSTc2dJ160836.2-392302	16:08:36.16	-39:23:02.88	-55.4 \pm 5.0	110.0 \pm 5.0	154	4205	1.15	2
Sz108B	16:08:42.86	-39:06:15.04	49.09 \pm 5.34	151.76 \pm 6.05	169	3125	0.11	1
J16085324-3914401	16:08:53.22	-39:14:40.53	60.72 \pm 4.00	100.31 \pm 5.47	168	3415	0.21	1
Sz111	16:08:54.67	-39:37:43.53	53.0 \pm 5.0	40.0 \pm 5.0	158	3705	0.21	2
Sz113	16:08:57.78	-39:02:23.21	10.78 \pm 9.19	147.36 \pm 14.20	163	3197	0.04	1
Sz114	16:09:01.83	-39:05:12.79	15.84 \pm 3.39	148.73 \pm 6.87	162	3175	0.21	1
J16102955-3922144	16:10:29.53	-39:22:14.83	66.54 \pm 9.21	118.86 \pm 9.49	163	3200	0.11	1
Sz123A	16:10:51.57	-38:53:14.17	43.0 \pm 5.0	145.0 \pm 5.0	159	3705	0.13	2
J16124373-3815031	16:12:43.73	-38:15:03.40	43.69 \pm 7.39	22.99 \pm 8.85	160	3705	0.39	1

NOTE—The coordinates were adopted from [Ansdell et al. \(2016\)](#), the inclination angle i and the position angle PA were adopted from (1) [Tazzari et al. \(2017\)](#) and (2) [Ansdell et al. \(2018\)](#). The distances were obtained by inverting the parallaxes measured by the Gaia mission ([Gaia Collaboration et al. 2016, 2018](#)). The luminosity L_{\star} and effective temperature T_{eff} of the stars were taken from [Alcalá et al. \(2014, 2017\)](#), according to the updated distances estimates ([Alcalá et al. 2019](#)). The distance for Sz123A could not be obtained from the Gaia data, therefore the mean distance to the Lupus Clouds was adopted.

that of the $J = 2-1$ emission at a lower frequency at a given temperature. Thus, we converted the intensity in our data from units of Jy beam^{-1} to brightness temperature in K to correct for this frequency dependence for direct comparison of different molecular lines and for the following analysis.

4. ANALYSIS

4.1. Stacking Molecular-Line Data

The S/Ns of the images of individual molecular lines are limited because of the short integration time of these surveys. Thus, we first stacked the data of different molecular lines to enhance the S/Ns. Different transitions of the same molecules are expected to trace a similar region in a disk, so we first stacked the $J = 2-1$ and $J = 3-2$ image cubes of ^{13}CO and

Table 2. Parameters adopted from the literature for the analysis for stars in the Taurus region

Name	RA	Dec	i	PA	dist	T_{eff}	L_{\star}
			[$^{\circ}$]	[$^{\circ}$]	[pc]	[K]	[L_{\odot}]
CITau	04:33:52.03	+22:50:29.81	50.0±0.3	11.2±0.4	158	4277	0.81
CIDA9A	05:05:22.82	+25:31:30.50	45.6±0.5	102.7±0.7	171	3589	0.20
DLTau	04:33:39.09	+25:20:37.79	45.0±0.2	52.1±0.4	159	4277	0.65
DNTau	04:35:27.39	+24:14:58.55	35.2 ^{+0.5} _{-0.6}	79.2±1.0	128	3806	0.70
DSTau	04:47:48.60	+29:25:10.76	65.2±0.3	159.6±0.4	159	3792	0.25
FTTau	04:23:39.20	+24:56:13.86	35.5±0.4	121.8±0.7	127	3444	0.15
GOTau	04:43:03.08	+25:20:18.35	53.9±0.5	20.9±0.6	144	3516	0.21
IPTau	04:24:57.09	+27:11:56.07	45.2 ^{+0.8} _{-0.9}	173.0±1.1	130	3763	0.34
IQTau	04:29:51.57	+26:06:44.45	62.1±0.5	42.4±0.6	131	3690	0.22
MWC480	04:58:46.27	+29:50:36.51	36.5±0.2	147.5±0.3	161	8400	17.38
RYTau	04:21:57.42	+28:26:35.09	65.0±0.1	23.1±0.1	128	6220	12.30
UZTauE	04:32:43.08	+25:52:30.63	56.1±0.4	90.4±0.4	131	3574	0.35
UZTauW	04:32:42.8	+25:52:31.2	61.2 ^{+1.1} _{-1.0}	91.5 ^{+0.8} _{-0.9}	131
BPTau	04:19:15.85	+29:06:26.48	38.2±0.5	151.1±1.0	129	3777	0.40
DOTau	04:38:28.60	+26:10:49.08	27.6±0.3	170.0±0.9	139	3806	0.23
DQTau	04:46:53.06	+16:59:59.89	16.1±1.2	20.3±4.3	197	3763	1.17
DRTau	04:47:06.22	+16:58:42.55	5.4 ^{+2.1} _{-2.6}	3.4 ^{+8.2} _{-8.0}	195	4205	0.63
GITau	04:33:34.07	+24:21:16.70	43.8±1.1	143.7 ^{+1.9} _{-1.6}	130	3792	0.49
GKTau	04:33:34.57	+24:21:05.49	40.2 ^{+5.9} _{-6.2}	119.9 ^{+8.9} _{-9.1}	129	4007	0.80
Har06-13	04:32:15.42	+24:28:59.21	41.1±0.3	154.2±0.3	130	4277	0.79
HOTau	04:35:20.22	+22:32:14.27	55.0±0.8	116.3±1.0	161	3386	0.14
HPTau	04:35:52.79	+22:54:22.93	18.3 ^{+1.2} _{-1.4}	56.5 ^{+4.6} _{-4.3}	177	4590	1.30
HQTau	04:35:47.35	+22:50:21.36	53.8±3.2	179.1 ^{+3.2} _{-3.4}	158	4900	4.34
V409Tau	04:18:10.79	+25:19:56.97	69.3±0.3	44.8±0.5	131	3763	0.66
V836Tau	05:03:06.60	+25:23:19.29	43.1±0.8	117.6±1.3	169	3734	0.44
DHTauA	04:29:41.56	+26:32:57.76	16.9 ^{+2.0} _{-2.2}	18.8 ^{+7.1} _{-7.2}	135	3516	0.20
DKTauA	04:30:44.25	+26:01:24.35	12.8 ^{+2.5} _{-2.8}	4.4 ^{+10.1} _{-9.4}	128	3902	0.45
DKTauB	04:30:44.4	+26:01:23.20	78.0 ^{+6.1} _{-11.0}	28.0 ^{+5.2} _{-5.4}	128
HKTauA	04:31:50.58	+24:24:17.37	56.9±0.5	174.9±0.5	133	3632	0.27
HKTauB	04:31:50.6	+24:24:15.09	83.2±0.2	41.2±0.2	133
HNTauA	04:33:39.38	+17:51:51.98	69.8 ^{+1.4} _{-1.3}	85.3 ^{+0.7} _{-0.6}	136	4730	0.16
RWAurA	05:07:49.57	+30:24:04.70	55.1 ^{+0.5} _{-0.4}	41.1±0.6	163	5250	0.99
RWAurB	05:07:49.5	+30:24:04.29	74.6 ^{+3.8} _{-8.2}	41.0 ^{+3.6} _{-3.7}	163
TTauN	04:21:59.45	+19:32:06.18	28.2±0.2	87.5±0.5	144	5250	6.82
TTauS	04:21:59.4	+19:32:05.52	61.6 ^{+8.8} _{-4.8}	7.9 ^{+3.7} _{-3.5}	144
UYAurA	04:51:47.40	+30:47:13.10	23.5 ^{+7.8} _{-6.6}	125.7 ^{+10.3} _{-10.9}	155	4060	1.05
V710TauA	04:31:57.81	+18:21:37.64	48.9±0.3	84.3±0.4	142	3603	0.26

NOTE—The coordinates, inclination angle i and position angle PA were adopted from Long et al. (2019). The effective temperature T_{eff} and luminosity L_{\star} were derived from Herczeg & Hillenbrand (2014) and were re-scaled for updated distances in Long et al. (2019). The parameters for secondary stars in binary systems were adopted from Manara et al. (2019). The distances were obtained by inverting the parallaxes measured by the Gaia mission (Gaia Collaboration et al. 2016, 2018).

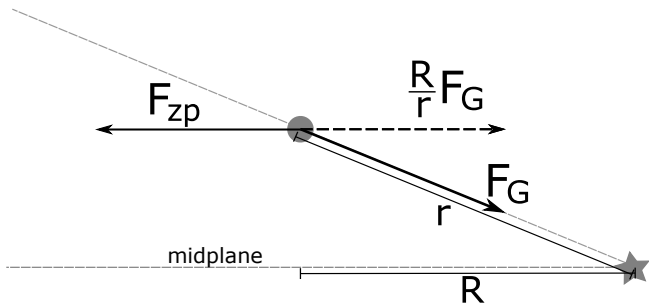


Figure 1. Geometry for calculating the central mass from the Keplerian orbit of gas in a disk around the star. r denotes the radius of the gas, R is the radius projected onto the midplane. F_G and F_{zp} are the gravitational and centripetal force, respectively.

of $C^{18}O$ for the YSOs in the Lupus star-forming region. The image cubes were combined by calculating the noise weighted mean of them. Hereafter, the images of the stacked $J = 2-1$ and $3-2$ data of ^{13}CO and $C^{18}O$ are called the ^{13}CO and $C^{18}O$ images, respectively. In addition, because different molecules in a disk are expected to follow the same Keplerian rotation, we also stacked the ^{13}CO , $C^{18}O$ and CN data with various combinations, hereafter $^{13}CO+CN$, $C^{18}O+CN$, $^{13}CO+C^{18}O$ and $^{13}CO+C^{18}O+CN$, to further achieve higher S/Ns. For the stars in the Taurus region no $J = 3-2$ and CN data was available. Therefore, only stacking of ^{13}CO and $C^{18}O$ $J = 2-1$ was possible.

We note that the different molecules may trace different regions in a disk, because of their different abundance distributions and opacities (Pinte et al. 2018). However, assuming the disk as an entity to be Keplerian, these different molecules still trace Keplerian motions in their respective regions. The mass of a YSO M_\star with gas orbiting in Keplerian motion with velocity v and at radius r can be calculated by

$$M_\star = \frac{r^2}{G} \frac{r}{R} \cdot \frac{v^2}{R}, \quad (1)$$

where G is the gravitational constant and R is the radius of the gas projected onto the disk midplane. The term r/R stems from decomposing the gravitational force, to obtain the force component parallel to the midplane. The geometry of the forces acting on the orbiting gas is shown in Figure 1. The radius of the gas r and its projected radius onto the midplane R are related by the height h of the emitting layer

$$r^2 = h^2 + R^2. \quad (2)$$

If the height h is small compared to the radius r , Equation 1 can be approximated by

$$M_\star = \frac{Rv^2}{G}. \quad (3)$$

Therefore, the mass derived with the actual radius of the orbit is different from the mass derived with the above approximation.

Performing the stacking of different molecules while neglecting their different scale heights might introduce additional uncertainties. However, these are typically small. For example, Pinte et al. (2018) found that the ^{13}CO emission in the disk around HD163296 is originating from a layer at an altitude of 25 au when the radius is 200 au. This results in an aspect ratio of the scale height of $h/R = 0.125$, assuming a linear relation between emitting height and radius. The deviation of the stellar mass calculated with the radius projected onto the disk midplane and calculated with the radius considering the scale height of $h/R = 0.125$, is less than 3% for a face-on disk. This effect was further tested on imaging simulations of disks with different inclination angles in Section 4.4. Due to the smaller optical depth of $C^{18}O$ compared to ^{13}CO , $C^{18}O$ is expected to trace regions closer to the midplane than ^{13}CO (Pinte et al. 2018), introducing a smaller error to the stellar mass by neglecting the height of the emitting layer.

Since the uncertainty due to the noise in the data is much larger than the errors due to different scale heights, which are only a few percent, stacking data of different molecular lines is not expected to influence the measurement noticeably. A detailed comparison of the measurements with different molecules is discussed in Section 5.3. The combination of molecular lines resulting in the highest S/N was used to obtain the final measurement of the stellar mass.

4.2. Measuring Stellar Mass

In this work, we measured the stellar masses by maximising auto-correction between the image cubes and various Keplerian rotational velocity patterns, as introduced by Yen et al. (2016, 2018). The principle of this method is the same as the Keplerian masking technique (e.g., Salinas et al. 2017; Teague et al. 2018b; Trapman et al. 2020). It makes use of the Keplerian motion of gas in protoplanetary disks around YSOs and corrects for the Doppler shift of the regions moving towards or away from an observer. The spectra at different positions in a disk are shifted by their Keplerian velocity projected onto the line of sight and stacked together. Different disk parameters are tested to find the parameters resulting in the stacked spectrum with the highest S/N, which is best corrected for the Doppler shift, and the disk parameters can be measured. Detailed descriptions of this method are given in Yen et al. (2016, 2018). Similar methods are also introduced in Teague et al. (2018b).

In our analysis, we adopted the assumption of a geometrically thin disk structure. Thus, the velocity pattern of a disk can be described by the six parameters, inclination angle (i), position angle (PA), stellar mass (M_\star), systemic velocity (v_{sys}), stellar position, and distance to a star. The stellar positions of our sample YSOs and PA and i of their disks have been measured with the continuum emission in the same data sets by Tazzari et al. (2017); Ansdell et al. (2018) and Long et al. (2019). Their parallaxes have been measured by the Gaia mission (Gaia Collaboration et al. 2016, 2018) and inverted to obtain their distances, except for Sz123A. The distances of our sample stars in the Lupus III cloud ranges from 137 pc to 169 pc with a median distance of 159 pc. We adopted this median distance to the Lupus III cloud of 159 pc for Sz123A in our analysis. We note that an uncertainty of 10% in the distance to Sz123A results in an uncertainty of 10% in its estimated stellar mass, which is not significant compared to the uncertainty due to the noise in the data.

Thus, there are only two unknown parameters, M_\star and v_{sys} in our analysis. All parameters adopted from the literature for this work are listed in Table 1 and Table 2 for the sources in the Lupus and Taurus star-forming regions, respectively. We note that actual disks have 3D structures, and our assumption of a geometrically thin disk structure could introduce errors in our analysis. These possible errors were evaluated by analysing synthetic images in Section 4.4.

For each source, we searched for a combination of M_\star and v_{sys} resulting in the velocity aligned stacked spectrum with the highest S/N. For each combination of the parameters, we generated a velocity aligned stacked spectrum averaged over the area from the center to a radius R in radial direction and from 0 to 2π in azimuthal direction, and measured its S/N. To measure the S/N, we first fitted a Gaussian line profile to the velocity aligned stacked spectrum, and calculated the S/N of the integrated intensity within a 1σ Gaussian line width. When the integrated intensity was computed, the included velocity channels were weighted with the fitted Gaussian line profile, so that more weight was put on the velocity channels near zero velocity with respect to v_{sys} . This is because when the adopted velocity pattern matches the actual disk rotation, the resultant stacked spectrum is symmetric and centred at zero velocity with respect to v_{sys} (Yen et al. 2016).

This weighting ensures that the narrower, more symmetrical spectrum has a higher S/N than other spectra with the same total flux but with a skewed profile, and is therefore favoured. The velocity alignment can also cause decorrelation of nearby pixels in an interferomet-

ric image, and thereby reduction of noise when large velocity shifts are applied (Yen et al. 2016). Therefore, the noise level of the original, non-aligned spectrum was adopted, when we measured the S/N to find the best-aligned spectrum. In this procedure, any velocity aligned stacked spectrum with the S/N at its peak below 4σ or with its line width narrower than three times the channel width was excluded from possible solutions to avoid false detections (Yen et al. 2018).

Because the radii of gaseous disks around our sample YSOs are not known, we first assumed R to be $1''$ for all the disks (Ansdell et al. 2018) and applied the analysis. After finding the parameters, which result in the best aligned spectrum, the radial intensity profile was extracted to measure the radius of the disk. We adopted the radius which encloses 95% of the total flux of the disk as the disk radius. This process of measuring the mass and determining the radial intensity profile was repeated until the change of the measured radius was less than 10%. The stellar mass itself is not sensible to the disk radius, but the uncertainty of the measurement of M_\star was reduced by adopting this measured disk radius. That is because when a radius larger or smaller than the actual disk radius was adopted in the analysis, additional noise or less signal were included.

We note that there could be cloud absorption in the spectra of our sources, as discussed in Ansdell et al. (2018) and Long et al. (2019). We examined all the spectra analyzed in this work and confirmed that there is no strong absorption in them (Appendix B). In addition, we performed tests on our analysis by arbitrarily masking a range of velocity channels to mimic cloud absorption, and we found that the best-fit results remain unchanged but the uncertainties increase. Thus, we expect that our results are not affected by possible cloud absorption.

4.3. Error Estimation

To estimate the uncertainty of our measurements, a series of velocity aligned stacked spectra were generated for each YSO by varying the disk parameters around the measurements. To include the uncertainty of the continuum measurements of the inclination and position angles, those parameters were also varied within their uncertainties. We did not consider the errors in the stellar position and distance, since their contributions are negligible compared to the errors in the inclination and position angles. These test spectra were compared against the best aligned spectrum with the highest S/N. We subtracted the test spectra from the best aligned spectrum and computed the χ^2 -value of the residual. On the assumption that the noise distribution in our

spectra follows a Gaussian function, the best aligned and test spectra were considered to be indistinguishable within the uncertainty, when the accumulated probability having a χ^2 smaller than the obtained value was 50%. Then the parameters used to generate these test spectra were also accepted as possible solutions. We defined the error bars as the highest and lowest values of the parameters resulting in a possible solution. This procedure sometimes suggests solutions consisting of very specific combinations of v_{sys} and M_* , which are isolated in the parameter space. These values were excluded if they had a probability of less than 2.5% in the number probability distributions of possible solutions.

This error estimation is different from that in Yen et al. (2018). In Yen et al. (2018), a Gaussian line profile was fitted to each test spectrum. When the center, peak intensity and width were all consistent with the best aligned spectrum and the difference in the S/Ns of the integrated fluxes was less than $\sqrt{2}$, the test spectrum was claimed to be indistinguishable from the best aligned spectrum. With imaging simulations (Section 4.4), we found that the method in Yen et al. (2018) tends to underestimate the errors, and our error estimate better represents the 1σ uncertainty of the measurements.

4.4. Robustness and Potential Bias

To test the robustness of our analysis and examine the potential bias due to our assumption of a geometrically thin disk, we used synthetic images in the ^{13}CO (3–2) emission of eight disk models with a stellar mass of $1.1 M_\odot$, which were generated by Miotello et al. (2016) using the physical and chemical code DALI (Bruderer et al. 2012; Bruderer 2013). The radial density structure was set by the characteristic radius $R_c = 60$ au and the power-law index $\gamma = 0.8$. The vertical density structure was varied by using different scale heights ($h_c = 0.1$ and 0.2), and flaring angles ($\psi = 0.1$ and 0.2 rad). Several values were adopted for the disk mass (10^{-1} , 10^{-3} , $10^{-5} M_\odot$). More details on the model parameters are given in Miotello et al. (2016). We projected each model at three different inclination angles (20° , 45° , and 80°) and simulated the ALMA observations on the model images to generate synthetic ALMA data cubes. Then we performed our analysis on these synthetic ALMA data. An example of our synthetic data and test is shown in Appendix C.

We found that the stellar mass could be overestimated by 20% to 30% with our method, when a disk is highly inclined ($i = 80^\circ$). For face-on disks ($i = 20^\circ$), the measured mass could be underestimated by less than 10%. For disks with moderate inclination, the measurements obtained from the synthetic data are consistent with the

model values. This is because the ^{13}CO (3–2) emission does not originate from the midplane but from an upper layer in a disk. This geometrical effect is most significant when a disk is close to face-on or edge-on, and our analysis could over- or underestimate the actual distance of the gas in the disk to the center. The effect on face-on disks is not notable because the uncertainties of the measurements are larger compared to this effect. For the seven YSOs with inclination angles larger than 70° in our sample, further analysis was done to verify their results (Section 6).

In addition, to test the robustness of our error estimation, we generated 700 synthetic ALMA data cubes from the disk models and included different random noise during the imaging simulations. These synthetic data cubes were analyzed with our method, and we obtained the probability distribution of the results. By comparing the distribution of the solutions to the error bars, we found that our error estimate indeed represents the 1σ uncertainty of our measurements.

5. RESULTS

We obtained measurements of the stellar mass for 28 out of 30 sources in the Lupus star forming region and for 17 out of 37 sources in the Taurus region with uncertainties ranging from $0.01 M_\odot$ to $0.33 M_\odot$ ($<10\%$ to 30%), and a mean uncertainty of $0.17 M_\odot$ (19%). For the sources for which we couldn't obtain a mass measurement, no alignment of the spectra could be found to meet our requirements (see Section 4.2). The final measurements, using the combination of molecular lines resulting in the highest S/N, are summarised in Tables 3 and 4 for the sources in Lupus and Taurus, respectively. The original and best aligned spectra averaged over the disk area from these combined data are shown in Appendix B. The distribution of the measured masses is shown in Appendix A.

5.1. Face-on Disks

When a disk is close to face-on, its millimeter continuum intensity distribution could appear nearly circular on the plane of sky, and the difference between its major and minor axes can be hard to detect. Thus, it can be difficult to measure the inclination and position angles of a disk which is nearly face-on with continuum data. The velocity pattern of a disk carries additional information and provides another way to measure the disk orientation.

In our sample, there are three nearly face-on disks with $i \leq 30^\circ$ in the Lupus region, Sz83, Sz113 and Sz114. In order to exploit the additional information provided by the velocity pattern of the gas, we measured PA and

Table 3. Final measurements for the sources in the Lupus region

Name	Molecular Line	M_*	v_{sys}	Disk Radius
		$[M_\odot]$	$[\text{km s}^{-1}]$	$[\text{au}]$
EXLup	^{13}CO	$0.86^{+0.36}_{-0.22}$	$4.15^{+0.25}_{-0.17}$	88
J15450887-3417333	$^{13}\text{CO}+\text{C}^{18}\text{O}$	0.25 ± 0.12	$4.84^{+0.51}_{-0.34}$	169
RXJ1556.1-3655	$^{13}\text{CO}+\text{C}^{18}\text{O}$	$0.75^{+0.14}_{-0.08}$	$5.19^{+0.17}_{-0.59}$	106
J16000236-4222145	$^{13}\text{CO}+\text{CN}+\text{C}^{18}\text{O}$	0.37 ± 0.04	4.09 ± 0.11	244
J16083070-3828268	^{13}CO	1.5 ± 0.15	$5.29^{+0.08}_{-0.25}$	284
J16085324-3914401	$^{13}\text{CO}+\text{CN}$	$0.43^{+0.11}_{-0.13}$	$3.72^{+0.11}_{-0.66}$	72
J16102955-3922144	$^{13}\text{CO}+\text{C}^{18}\text{O}$	0.19 ± 0.03	$3.52^{+0.09}_{-0.17}$	189
J16124373-3815031	$^{13}\text{CO}+\text{CN}$	$0.77^{+0.26}_{-0.15}$	$4.36^{+0.22}_{-0.44}$	90
MYLup	$^{13}\text{CO}+\text{CN}+\text{C}^{18}\text{O}$	$1.49^{+0.15}_{-0.17}$	$4.78^{+0.22}_{-0.44}$	187
RYLup	$^{13}\text{CO}+\text{C}^{18}\text{O}$	1.5 ± 0.15	$3.67^{+0.68}_{-0.25}$	174
Sz100	$^{13}\text{CO}+\text{CN}$	$0.29^{+0.04}_{-0.05}$	1.76 ± 0.11	92
Sz108B	$^{13}\text{CO}+\text{CN}+\text{C}^{18}\text{O}$	$0.13^{+0.03}_{-0.05}$	$2.54^{+0.11}_{-0.33}$	113
Sz111	$^{13}\text{CO}+\text{C}^{18}\text{O}$	0.61 ± 0.06	$4.15^{+0.09}_{-0.17}$	203
Sz114	$^{13}\text{CO}+\text{CN}+\text{C}^{18}\text{O}$	$0.32^{+0.25}_{-0.14}$	4.91 ± 0.11	125
Sz123A	$^{13}\text{CO}+\text{C}^{18}\text{O}$	$0.46^{+0.09}_{-0.08}$	$4.29^{+0.08}_{-0.34}$	122
Sz129	$^{13}\text{CO}+\text{CN}+\text{C}^{18}\text{O}$	$0.85^{+0.12}_{-0.14}$	$4.16^{+0.11}_{-0.33}$	106
Sz133	$^{13}\text{CO}+\text{CN}+\text{C}^{18}\text{O}$	$1.23^{+0.15}_{-0.12}$	$3.92^{+0.33}_{-0.11}$	259
Sz65	^{13}CO	$1.14^{+0.24}_{-0.13}$	$4.44^{+0.26}_{-0.34}$	161
Sz69	^{13}CO	0.22 ± 0.12	$5.5^{+0.17}_{-0.51}$	104
Sz71	$^{13}\text{CO}+\text{CN}+\text{C}^{18}\text{O}$	0.46 ± 0.05	3.62 ± 0.11	194
Sz73	^{13}CO	0.86 ± 0.23	$4.49^{+0.08}_{-0.34}$	114
Sz75	^{13}CO	0.96 ± 0.1	$2.76^{+0.34}_{-0.17}$	129
Sz76	$^{13}\text{CO}+\text{C}^{18}\text{O}$	0.14 ± 0.03	$3.64^{+0.09}_{-0.17}$	144
Sz83	^{13}CO	$1.0^{+0.63}_{-0.47}$	$4.68^{+0.08}_{-0.17}$	154
Sz84	$^{13}\text{CO}+\text{C}^{18}\text{O}$	$0.96^{+0.19}_{-0.1}$	$4.82^{+0.51}_{-0.26}$	158
Sz90	$^{13}\text{CO}+\text{CN}$	$1.05^{+0.1}_{-0.45}$	$5.24^{+0.44}_{-0.55}$	93
Sz98	$^{13}\text{CO}+\text{CN}$	1.05 ± 0.1	$3.05^{+0.11}_{-0.22}$	206
SSTc2dJ160836.2-392302	^{13}CO	1.06 ± 0.11	5.39 ± 0.08	389

i of these nearly face-on sources using the ^{13}CO data with our analysis. In addition to the mass and systemic velocity of the YSOs, PA and i were also varied from 0° to 180° in steps of 5° and from 3° to 30° in steps of 2° , respectively, to search for the combination to best align their spectra. Then, we followed the same procedure as described above to obtain the measurements, including i and PA , and their uncertainties.

Our estimated i and PA for Sz83 deviate from the measurements from the continuum by 13° and 44° , which are 2.2σ and 2.7σ differences, respectively. The deviations for Sz114 are $< 5^\circ$ and 11° for i and PA , respectively, which is less than 1σ for both quantities. With the disk orientations measured from the molecular line data, we could properly align the spectra, with S/Ns

above 17 in Sz83 and Sz114. However, we still could not find any detection in Sz113, even after we considered different disk orientations.

For the nearly face-on disks in the Taurus region, no significant difference between the orientations measured with continuum or line emission data was found, and the orientations measured with the continuum emission were adopted in our analysis to obtain the measurements of stellar mass and systemic velocity. The position and inclination angles measured from the ^{13}CO data for the nearly face-on sources in the Lupus region are listed in Table 5.

5.2. Dependence on Disk Properties

Table 4. Final measurements for the sources in the Taurus region

Name	Molecular Line	M_*	v_{sys}	Disk Radius
		[M_\odot]	[km s^{-1}]	[au]
CIDA9A	$^{13}\text{CO}+\text{C}^{18}\text{O}$	0.78 ± 0.08	$6.5^{+0.08}_{-0.17}$	123
DOTau	$^{13}\text{CO}+\text{C}^{18}\text{O}$	0.54 ± 0.07	$6.02^{+0.08}_{-0.09}$	202
DQTau	$^{13}\text{CO}+\text{C}^{18}\text{O}$	$2.85^{+0.77}_{-0.72}$	9.1 ± 0.17	83
DRTau	$^{13}\text{CO}+\text{C}^{18}\text{O}$	$1.18^{+0.59}_{-0.44}$	$9.9^{+0.08}_{-0.09}$	246
DSTau	$^{13}\text{CO}+\text{C}^{18}\text{O}$	1.08 ± 0.11	5.7 ± 0.17	129
FTTau	$^{13}\text{CO}+\text{C}^{18}\text{O}$	$0.35^{+0.04}_{-0.06}$	$7.22^{+0.09}_{-0.08}$	129
HKTauA	$^{13}\text{CO}+\text{C}^{18}\text{O}$	$0.49^{+0.06}_{-0.05}$	$5.98^{+0.09}_{-0.51}$	63
HKTauB	$^{13}\text{CO}+\text{C}^{18}\text{O}$	$1.23^{+0.26}_{-0.12}$	$6.05^{+0.7}_{-0.37}$	69
HOTau	$^{13}\text{CO}+\text{C}^{18}\text{O}$	$0.44^{+0.05}_{-0.16}$	$6.38^{+0.09}_{-0.51}$	102
IPTau	$^{13}\text{CO}+\text{C}^{18}\text{O}$	$0.8^{+0.23}_{-0.22}$	$6.87^{+0.25}_{-0.6}$	49
IQTau	$^{13}\text{CO } J = 2-1$	$0.42^{+0.05}_{-0.15}$	$5.5^{+0.34}_{-0.25}$	108
MWC480	$^{13}\text{CO } J = 2-1$	2.16 ± 0.22	$5.13^{+0.09}_{-0.08}$	355
RWAurA	$^{13}\text{CO}+\text{C}^{18}\text{O}$	$1.4^{+0.28}_{-0.14}$	$5.84^{+0.65}_{-0.58}$	59
TTauN	$\text{C}^{18}\text{O } J = 2-1$	$2.06^{+0.66}_{-0.43}$	$9.1^{+0.17}_{-0.42}$	152
UZTauE	$^{13}\text{CO } J = 2-1$	1.21 ± 0.12	$5.7^{+0.08}_{-0.17}$	140
V710Tau	$^{13}\text{CO}+\text{C}^{18}\text{O}$	$0.58^{+0.06}_{-0.07}$	6.5 ± 0.17	72
V836Tau	$^{13}\text{CO}+\text{C}^{18}\text{O}$	$0.92^{+0.22}_{-0.2}$	$7.18^{+0.42}_{-0.43}$	71

As discussed in Section 4.4, when the inclination of a disk is close to face-on or edge-on, our analysis could under- or overestimate the stellar mass. Other possible biases could be introduced by larger disk radii, higher disk mass or higher surface density. A flared disk has a larger height at an outer radius, and the opacity of a disk increases with a higher surface density or disk mass. These could cause the emission lines to trace an upper layer of a disk and result in a larger deviation from the geometrically-thin disk approximation.

To examine these possible biases in our measurements, Figure 2 compares the ratios of our measured dynamical masses to the spectroscopic masses estimated and the stellar evolutionary model by Baraffe et al. (2015) with the inclination angles, outer radii, masses, and mean surface densities of the sample disks. The outer radius of a disk is defined as the radius enclosing 95% of the total flux. The outer radii of our sample disks were measured in our analysis in Section 4.2. The disk gas masses were measured by Ansdell et al. (2016) using the ^{13}CO and $\text{C}^{18}\text{O } J = 3-2$ emission lines. The mean surface densities were estimated from the disk gas masses and outer radii. Because there are no measurements of the disk masses of the Taurus sources available in the literature, we did not include the Taurus sources in the comparison with the

disk masses and mean surface densities. Details about the stellar evolutionary models are given in Section 6.

There is no clear relation between the ratio of the dynamical and spectroscopic stellar masses and these disk properties in Figure 2, suggesting that the effect caused by the geometrically-thin disk approximation is less than the uncertainty of our measurements. The comparisons of the disk properties with the ratio of the dynamical and spectroscopic stellar masses were also made for the other stellar evolutionary models mentioned in Section 6. No clear relation was found for any of the models. Therefore, our comparison and discussion on the dynamical and spectroscopic masses in Section 6 are not biased by these effects. However, since the last data points at high inclination angles in Figure 2a hint at an overestimation of stellar mass, which was also found with the synthetic data, our measurements of the disks with inclination angles larger than 70° should be interpreted with caution.

5.3. Measurements with Individual Lines

We obtained 42 and 22 measurements out of the total sample of 67 YSOs using the ^{13}CO and C^{18}O data, respectively. Furthermore, we obtained 26 measurements of the stellar mass with the CN data for the sources in the Lupus region. For HOTau we could only obtain a measurement using the stacked $^{13}\text{CO}+\text{C}^{18}\text{O}$ data. The results of the measurements using the individual line data for the Lupus region are shown in Table 6, and in Table 7 for the sources in the Taurus region. The results obtained with the different molecular lines are compared in the graphs displayed in Figure 3. 80% of the measurements from different line data agree on a level better than 1σ and 16% agree on a level of 1 to 2σ . Only 4% of the measurements show deviations on a level between 2σ and 3.5σ . On average, the deviations are within a 0.5σ level. Therefore, our measurements obtained with data of different molecular lines do not show significant deviations. This demonstrates that possible differences in emitting regions of these molecular lines in a disk are negligible in our analysis, and stacking different molecular line data does not introduce a bias to our analysis and can increase the S/Ns of our measurements.

5.4. Comparison with Literature

Yen et al. (2018) applied the same analysis on the ^{13}CO and $\text{C}^{18}\text{O } J = 3-2$ data obtained with the same ALMA observations. The Band 6 data were not available yet. By stacking the ^{13}CO and $\text{C}^{18}\text{O } (3-2 \text{ \& } 2-1)$ and CN data, we obtained six more measurements, compared to Yen et al. (2018). Although the new error estimation is less restrictive than the one used in Yen et al. (2018), the uncertainty decreased on average by 18%.

Table 5. Measured parameters for face-on disks in the Lupus region

Name	RA	Dec	i	PA	dist
			[$^{\circ}$]	[$^{\circ}$]	[pc]
Sz83	15:56:42.29	-37:49:15.82	$16.0^{+6.0}_{-4.0}$	120.0 ± 15.0	160
Sz113	16:08:57.78	-39:02:23.21	163
Sz114	16:09:01.83	-39:05:12.79	$16.0^{+6.0}_{-4.0}$	$160.0^{+25.0}_{-10.0}$	162

NOTE—We measured the inclination and position angles with the molecular-line data for face-on disks whose inclination angles were measured to be $\leq 30^{\circ}$ with the continuum data.

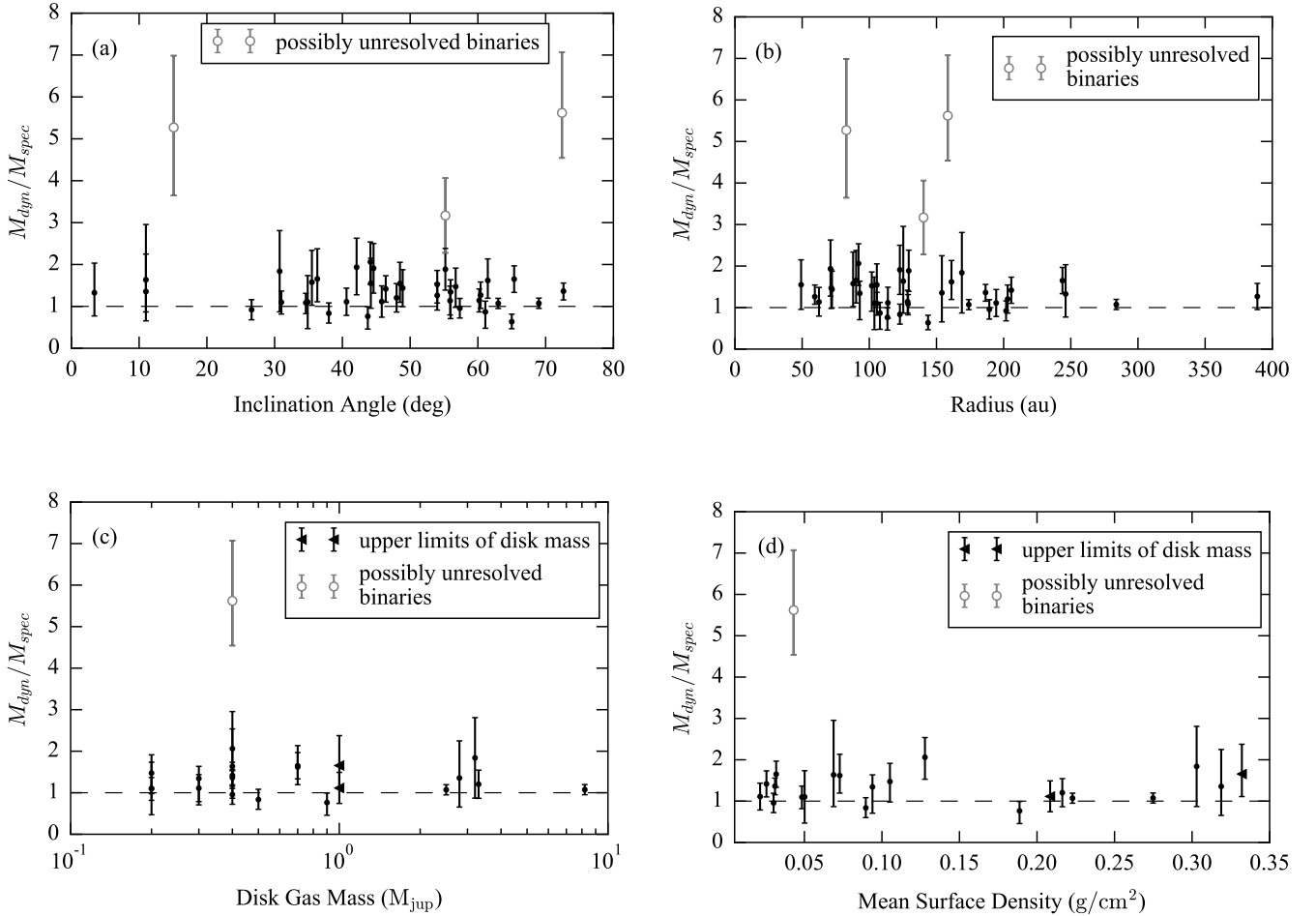


Figure 2. Ratio between our measurements of dynamical stellar masses M_{dyn} and the spectroscopically determined stellar masses M_{spec} as a function of different disk properties: (a) the inclination angle, (b) the radius, (c) the disk gas mass and (d) the mean surface density. No clear dependence on the disk properties is observable. In Figures (c) and (d) only sources in the Lupus star-forming region are included, for which the disk masses were measured by [Ansdell et al. \(2016\)](#). The stars, marked with grey circles, are found to be possibly unresolved binaries (see Section 6.1). Triangles indicate upper limits of the disk mass.

Table 6. Measurements of the individual line data for the sources in the Lupus region

Name	^{13}CO		C^{18}O		CN	
	M_\star [M_\odot]	v_{sys} [km s^{-1}]	M_\star [M_\odot]	v_{sys} [km s^{-1}]	M_\star [M_\odot]	v_{sys} [km s^{-1}]
EXLup	$0.86^{+0.36}_{-0.22}$	$4.15^{+0.25}_{-0.17}$	$0.81^{+0.23}_{-0.17}$	3.64 ± 0.25	0.58 ± 0.31	$4.59^{+0.11}_{-0.99}$
J15450887-3417333	$0.2^{+0.1}_{-0.07}$	$4.84^{+0.34}_{-0.17}$	$0.2^{+0.21}_{-0.16}$	$4.62^{+0.22}_{-0.55}$
RXJ1556.1-3655	$0.75^{+0.14}_{-0.08}$	$5.19^{+0.17}_{-0.51}$	$0.69^{+0.13}_{-0.38}$	$5.19^{+0.08}_{-0.77}$	$0.65^{+0.1}_{-0.06}$	$4.75^{+0.55}_{-0.22}$
J16000236-4222145	0.44 ± 0.04	$4.01^{+0.09}_{-0.08}$	0.31 ± 0.03	4.09 ± 0.11
J16083070-3828268	1.5 ± 0.15	$5.29^{+0.08}_{-0.25}$	$1.5^{+0.54}_{-0.22}$	$4.86^{+0.68}_{-0.34}$	1.38 ± 0.14	$5.18^{+0.11}_{-0.33}$
J16085324-3914401	$0.33^{+0.12}_{-0.08}$	$3.63^{+0.58}_{-0.49}$	$0.31^{+0.03}_{-0.17}$	$3.38^{+0.11}_{-0.99}$
J16102955-3922144	$0.18^{+0.05}_{-0.03}$	$3.6^{+0.08}_{-0.17}$	$0.2^{+0.04}_{-0.14}$	$3.86^{+0.34}_{-0.59}$	$0.17^{+0.06}_{-0.03}$	$3.52^{+0.22}_{-0.33}$
J16124373-3815031	$0.66^{+0.2}_{-0.12}$	$4.58^{+0.22}_{-0.77}$
MYLup	1.79 ± 0.45	$4.86^{+0.46}_{-0.57}$	$1.37^{+0.25}_{-0.14}$	$4.78^{+0.22}_{-0.55}$
RYLup	$1.44^{+0.17}_{-0.14}$	$3.84^{+0.42}_{-0.34}$	$1.62^{+0.78}_{-0.16}$	$4.18^{+1.72}_{-1.15}$	$1.23^{+0.27}_{-0.12}$	$3.45^{+0.44}_{-0.55}$
Sz100	$0.26^{+0.04}_{-0.05}$	1.76 ± 0.17	$0.08^{+0.04}_{-0.02}$	$1.6^{+0.17}_{-0.43}$	0.21 ± 0.05	$1.88^{+0.11}_{-0.22}$
Sz108B	0.1 ± 0.04	$2.46^{+0.08}_{-0.17}$	0.16 ± 0.06	$2.46^{+0.25}_{-0.17}$	0.1 ± 0.04	$2.54^{+0.22}_{-0.33}$
Sz111	0.6 ± 0.06	$4.15^{+0.08}_{-0.17}$	$0.58^{+0.21}_{-0.32}$	$4.32^{+0.43}_{-0.59}$	$0.46^{+0.07}_{-0.09}$	$3.93^{+0.11}_{-0.22}$
Sz114	$0.34^{+0.21}_{-0.16}$	4.82 ± 0.08	$0.3^{+0.19}_{-0.15}$	4.58 ± 0.11
Sz123A	$0.44^{+0.1}_{-0.09}$	$4.29^{+0.08}_{-0.34}$	$0.44^{+0.12}_{-0.13}$	3.96 ± 0.22
Sz129	$1.01^{+0.2}_{-0.26}$	$4.16^{+0.25}_{-0.42}$	0.72 ± 0.15	$4.16^{+0.11}_{-0.33}$
Sz133	1.63 ± 0.59	$3.66^{+0.37}_{-0.75}$	$1.09^{+0.17}_{-0.11}$	$3.92^{+0.44}_{-0.11}$
Sz65	$1.14^{+0.24}_{-0.13}$	$4.44^{+0.26}_{-0.34}$	$1.39^{+0.5}_{-0.33}$	$4.56^{+0.47}_{-0.62}$
Sz69	0.22 ± 0.12	$5.5^{+0.17}_{-0.51}$
Sz71	0.46 ± 0.05	3.62 ± 0.08	0.45 ± 0.05	3.52 ± 0.11
Sz73	0.86 ± 0.23	$4.49^{+0.08}_{-0.34}$	$0.74^{+0.18}_{-0.27}$	3.72 ± 0.33
Sz75	0.96 ± 0.1	$2.76^{+0.34}_{-0.17}$
Sz76	0.15 ± 0.03	$3.64^{+0.08}_{-0.17}$	$0.25^{+0.09}_{-0.06}$	$3.81^{+0.34}_{-0.43}$	$0.13^{+0.03}_{-0.05}$	$3.53^{+0.11}_{-0.22}$
Sz83	$1.0^{+0.63}_{-0.47}$	$4.68^{+0.08}_{-0.17}$	$1.12^{+0.7}_{-0.53}$	$4.6^{+0.08}_{-0.42}$	$1.02^{+0.64}_{-0.62}$	4.35 ± 0.22
Sz84	$1.03^{+0.18}_{-0.1}$	$5.16^{+0.25}_{-0.51}$	$0.98^{+0.21}_{-0.16}$	$4.82^{+0.34}_{-0.42}$	$0.82^{+0.3}_{-0.08}$	$5.04^{+0.33}_{-0.55}$
Sz90	$0.41^{+0.04}_{-0.22}$	$5.5^{+0.6}_{-0.25}$	$1.19^{+0.43}_{-0.86}$	$5.24^{+0.77}_{-0.44}$
Sz98	$0.78^{+0.14}_{-0.11}$	2.96 ± 0.08	1.05 ± 0.1	$3.05^{+0.11}_{-0.33}$
SSTc2dJ160836.2-392302	1.06 ± 0.11	5.39 ± 0.08	$1.0^{+0.14}_{-0.1}$	$5.3^{+0.17}_{-0.08}$	1.15 ± 0.11	5.5 ± 0.11

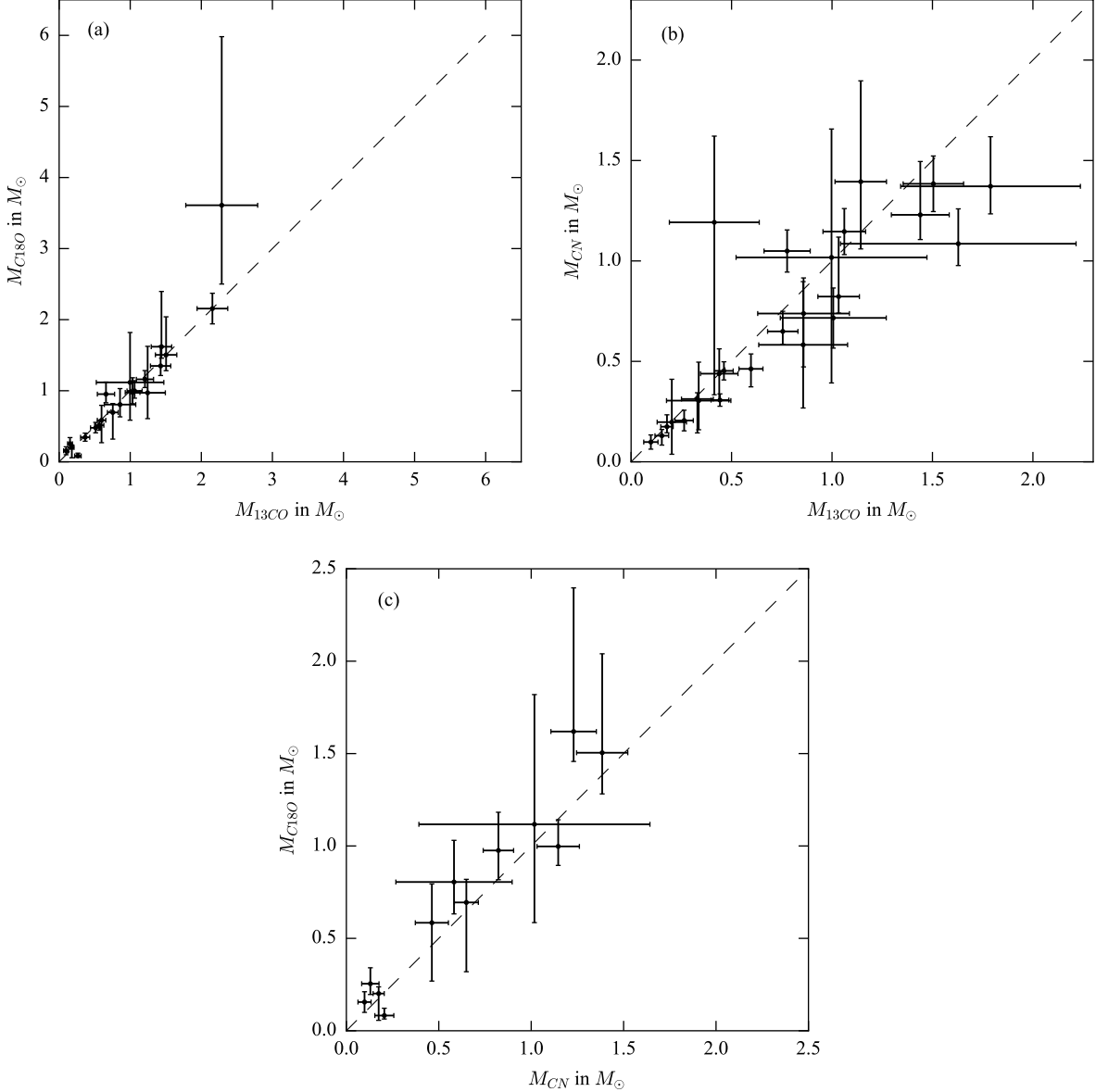


Figure 3. Comparison between the results of the mass measurement using different molecular lines. Comparison of the measurements obtained with (a) the ^{13}CO and $C^{18}O$ data, (b) the ^{13}CO and CN data and (c) the CN and $C^{18}O$ data.

Sz68, which was detected in [Yen et al. \(2018\)](#), could not be detected in this work with higher S/N data, and thus it could be a false detection in [Yen et al. \(2018\)](#). For the sources detected in both works, all measurements are consistent within the 2σ uncertainty, except Sz84, for which the deviation is 3.4σ .

Eleven of our detected sources were also studied by [Simon et al. \(2000, 2019\)](#). In those studies, disk models were fitted to the velocity channel maps in the visibility domain to measure the dynamical stellar mass. The results depend on the adopted inclination angle and distance. To compare our results with the literature, the measured stellar masses in the literature were scaled

with the distances and inclination angles adopted in our analysis. The relation of stellar mass M_{\star} , inclination angle i and distance D is as follows ([Simon et al. 2000](#)):

$$M_{\star} \propto \frac{D}{\sin^2 i} \quad (4)$$

The stellar masses obtained from the literature after scaling are listed in Table 8. For seven out of the eleven (64%) sources, our results agree with the literature on a level better than 1σ . There are two and one YSOs with their results consistent with the literature within 2σ and 3σ , respectively. The only exception is IQTau, where our estimated stellar mass is 50% different from

Table 7. Measurements of the individual line data for the sources in the Taurus region

Name	$^{13}\text{CO } J = 2-1$		$\text{C}^{18}\text{O } J = 2-1$	
	M_*	v_{sys}	M_*	v_{sys}
	$[M_\odot]$	$[\text{km s}^{-1}]$	$[M_\odot]$	$[\text{km s}^{-1}]$
CIDA9A	0.78 ± 0.08	$6.50^{+0.09}_{-0.17}$	$0.95^{+0.17}_{-0.12}$	6.33 ± 0.17
DOTau	0.51 ± 0.07	$6.02^{+0.08}_{-0.09}$	$0.48^{+0.08}_{-0.07}$	$6.02^{+0.08}_{-0.09}$
DQTau	$2.29^{+0.72}_{-0.51}$	9.1 ± 0.34	$3.61^{+2.37}_{-1.11}$	$9.27^{+0.6}_{-0.17}$
DRTau	1.24 ± 0.25	$9.9^{+0.08}_{-0.09}$	$0.97^{+0.65}_{-0.36}$	$9.9^{+0.08}_{-0.09}$
DSTau	0.99 ± 0.1	5.7 ± 0.17
FTTau	$0.37^{+0.04}_{-0.06}$	$7.22^{+0.09}_{-0.08}$	0.34 ± 0.06	$7.22^{+0.09}_{-0.17}$
HKTauA	$0.52^{+0.05}_{-0.06}$	$5.98^{+0.09}_{-0.34}$
HKTauB	$1.18^{+0.29}_{-0.12}$	$6.9^{+0.26}_{-0.59}$
HOTau
IPTau	$0.4^{+0.13}_{-0.05}$	$7.04^{+0.08}_{-0.51}$
IQTau	$0.42^{+0.05}_{-0.15}$	$5.5^{+0.34}_{-0.25}$
MWC480	2.16 ± 0.22	$5.13^{+0.09}_{-0.08}$	2.16 ± 0.22	$5.04^{+0.09}_{-0.08}$
RWAurA	$1.43^{+0.2}_{-0.14}$	$5.5^{+0.46}_{-0.38}$	$1.35^{+0.28}_{-0.13}$	$6.86^{+0.38}_{-0.76}$
TTauN	$2.06^{+0.66}_{-0.43}$	$9.1^{+0.17}_{-0.42}$
UZTauE	1.21 ± 0.12	$5.7^{+0.08}_{-0.17}$	1.16 ± 0.12	$5.7^{+0.25}_{-0.17}$
V710Tau	0.56 ± 0.06	$6.5^{+0.17}_{-0.25}$	0.51 ± 0.07	$6.5^{+0.08}_{-0.17}$
V836Tau	$0.66^{+0.2}_{-0.12}$	$7.18^{+0.42}_{-0.43}$

the literature, which is 4.7σ difference. The comparisons of our results with the literature are displayed in Figure 4. By calculating the percental deviations of our results and the results of Simon et al. (2000, 2019), we found an average deviation of $0.33^{+4.6}_{-7.5}\%$. Thus, our analysis on the data with much lower S/Ns to measure the stellar mass dynamically yields consistent results.

6. DISCUSSION

6.1. Unresolved Binaries

In order to examine the stellar evolutionary models, we obtained the dynamical stellar masses of 45 YSOs in the Lupus and Taurus star-forming regions. By comparing their dynamically and spectroscopically determined stellar masses, we can assess the accuracy of the stellar evolutionary models. We note that such a comparison can be biased if unresolved binaries are included in our sample. In the case of an unresolved binary system, the dynamical mass measurement includes the total mass of both stars. The estimated spectroscopic mass depends on how the temperature and luminosity of the stars add up. The measured luminosity of an unresolved binary system is the combined luminosity of both stars, while the spectral types, and therefore the effective tempera-

Table 8. Dynamically determined stellar masses obtained from the literature and re-scaled values

Name	M_{pub}	i_{pub}	dist_{pub}	M_*	Ref.
	$[M_\odot]$	$[\circ]$	$[\text{pc}]$	$[M_\odot]$	
Simon et al. (2000)					
MWC480	1.65 ± 0.07	38	140	2.035 ± 0.007	
UZTauE	1.31 ± 0.08	56	140	1.23 ± 0.08	
Simon et al. (2019)					
IPTau	0.94 ± 0.05	34	130	0.58 ± 0.03	1
IQTau	0.74 ± 0.02	57.9	131	0.68 ± 0.02	2
HKTauA	0.53 ± 0.03	51	133	0.46 ± 0.03	1
HKTauB	0.89 ± 0.04	81	133	0.88 ± 0.04	1
V710Tau	0.67 ± 0.06	46	142	0.61 ± 0.05	1
HOTau	0.43 ± 0.03	64	161	0.52 ± 0.04	1
DSTau	0.83 ± 0.02	71	158	0.9 ± 0.02	1
MWC480	2.11 ± 0.06	...	161	2.11 ± 0.06	3
CIDA9A	1.32 ± 0.24	33	171	0.77 ± 0.14	1

NOTE— M_{pub} , i_{pub} , dist_{pub} are dynamical stellar mass, inclination angle, and distance in the literature, respectively. M_* is the stellar mass, scaled to have the same inclination angle and distance as those in our study. References for the inclination angles adopted in Simon et al. (2019): 1) Simon et al. (2017), 2) Guilloteau et al. (2014), 3) the originally adopted inclination angle could not be found in the literature.

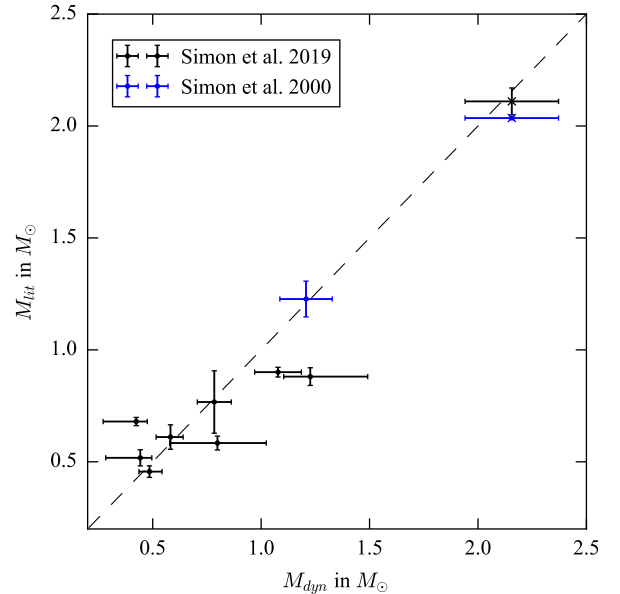


Figure 4. Comparison of our results M_{dyn} and the dynamical mass measurements in the literature M_{lit} (Simon et al. 2000, 2019). The data points marked with crosses denote MW480, which was measured in both papers.

tures of the stars, do not add up directly. When fitting the binary system’s spectrum with a template spectrum of a single star, the typical error in the estimated effective temperature of the primary star is around 300 K, and the error depends on the mass ratio of primary and secondary stars (El-Badry et al. 2018). Since the evolutionary tracks for low mass stars are close to vertical in the HR diagram, the errors in the effective temperature directly transfer to be the errors in the derived stellar masses. Thus, the dynamical mass can be significantly higher than the spectroscopic mass for unresolved binaries, in addition to the inaccuracies in the stellar evolutionary model. In order to identify possible unresolved binaries in our sample, we first divided the effective temperatures in our sample into five ranges and calculated the median dynamical stellar mass per section. If the dynamical mass of a star in our sample deviates from the median mass by more than three times the median absolute deviation (mad), we consider this source a possible unresolved binary system.

In Figure 5, the locations of our sample sources in the HR diagram are shown. Three sources in our sample were found to have a large deviation from the median stellar mass. Sz84 deviates by 11.0 mad from the median stellar mass, which corresponds to a deviation of 278%. This object is highly inclined ($i = 73.99 \pm 1.56$), which might cause an additional overestimation of the stellar mass (see Section 4.4). UZTauE and DQTau deviate by 3.7 mad (103%) and 13.6 mad (379%), respectively. These candidates of unresolved binaries are marked with diamond shaped markers in Figure 5. Indeed, we note that other observations in the literature have confirmed that UZTauE and DQTau are binary systems (Prato et al. 2002; Mathieu et al. 1997). Thus, these three sources are excluded in the following comparison of the spectroscopic and dynamical mass measurements.

6.2. Comparison between Dynamical and Spectroscopic Mass Measurements

We compare our measured dynamical stellar masses with spectroscopic stellar masses estimated with seven different stellar evolutionary models, developed by Palla & Stahler (1999, 1993), Siess et al. (2000), Bressan et al. (2012), Chen et al. (2014) and Baraffe et al. (2015), hereafter PS99, SFD00, Br12, C14 and BHAC15, respectively, as well as by Feiden (2016). Feiden (2016) includes two evolutionary models, one without and one with the influence of magnetic fields, hereafter F16 and the magnetic F16, respectively. The spectroscopic masses were calculated using the values given in Table 1 and 2. For PS99 and SFD00 an uncertainty of 15% was adopted. For the other evolutionary models the uncer-

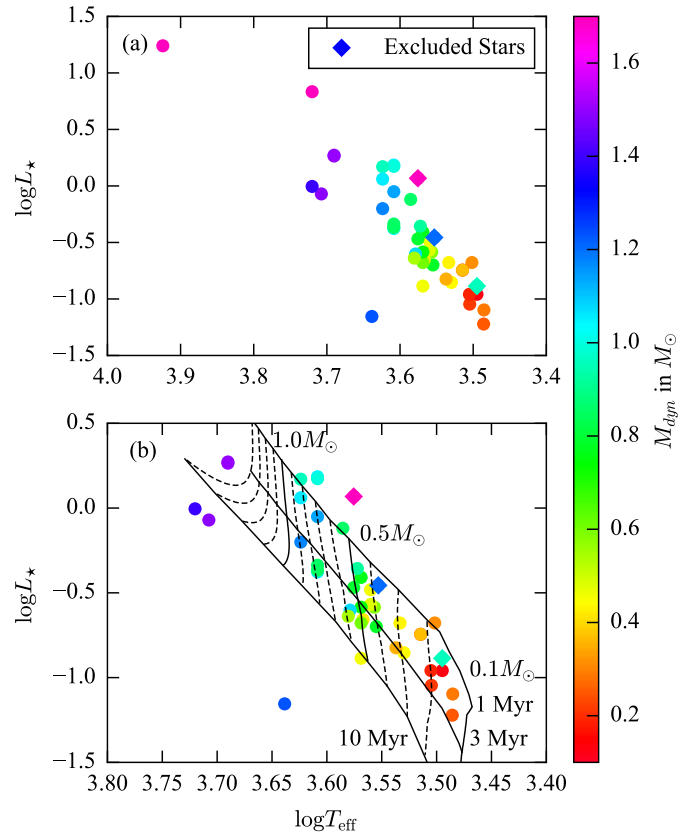


Figure 5. Locations of our sample sources in the HR diagram. Colours of the symbols present their dynamical stellar masses. Diamonds denote the candidates of unresolved binaries. In (a), the complete sample is shown, and (b) enlarges the region of ~ 2500 K to 6300 K and shows exemplarily the 1, 3 and 10 Myr isochrones of the evolutionary model of Baraffe et al. (2015).

tainty was estimated by calculating the probability distribution of the derived stellar mass, considering the errors of luminosity and effective temperature. The mass range around the median containing 68% of the distribution was adopted as the uncertainty. The typical uncertainty of 20% in luminosity and 2.5% for an effective temperature $T_{\text{eff}} < 3500$ K and 4.5% for $T_{\text{eff}} > 3500$ K was adopted in the calculations. The mean uncertainty of the spectroscopic mass in our sample is $0.1 M_{\odot}$. All calculated values for the spectroscopic models are given in Table 11 and Table 12 in Appendix D. As already noted in several works (e.g., Alcalá et al. 2014, 2017), a small number of stars are found on the HR diagram to be well below the 10 Myr isochrone. Several reasons can lead to these effects, but most probably this is due to dust obscuration by an edge-on disk (Alcalá et al. 2014, 2017)

The adopted stellar evolutionary models are often used in the literature (e.g. Hillenbrand & White (2004); Stassun et al. (2014); Herczeg & Hillenbrand (2015); Manara et al. (2017)). These models differ in the adopted surface boundary conditions and equation of state. C14, F16 and BHAC15 adopted non-gray boundary conditions, while PS99 and Br12 adopted gray boundary conditions. Gray boundary conditions assume constant opacity and neglect the frequency dependence. This approximation can be used for higher mass stars, but causes inaccuracies for lower mass stars. SFD00 adopted semi-gray boundary conditions, which is an analytical fit to the thermal structure of a non-grey atmosphere. All models use the mixing length theory to describe convection, but adopt different mixing length parameters.

Figure 6 presents the difference between the spectroscopic and dynamical stellar masses in ratio for different stellar evolutionary models. For individual stars, we found that the spectroscopic measurements are consistent with the dynamical masses within 3σ for most stars. No star shows a difference between spectroscopic and dynamical masses more than 5σ , except for the stars which are possibly unresolved binaries (see Section 6.1). Nevertheless, possible systematic trends are seen in Figure 6. To examine if there is any significant trend between the spectroscopic and dynamical masses in our sample, we separated our sample sources into three different mass ranges, low ($M_\star \leq 0.6 M_\odot$), intermediate ($0.6 M_\odot \leq M_\star \leq 1.3 M_\odot$) and high ($M_\star \geq 1.3 M_\odot$) mass stars. These three mass ranges contain 17, 19 and 6 stars, respectively. The mass ranges are chosen based on Figure 6 and possibly exhibit the largest deviations between spectroscopic and dynamical masses for most of the stellar evolutionary models. Then we computed the mean differences between the spectroscopic and dynamical masses in these mass ranges as well as the uncertainties of the mean differences. The uncertainties of the mean differences were calculated by propagating the errors of the individual measurements of dynamical and spectroscopic masses. The results are listed in Table 9.

In the low mass range, the spectroscopic masses from the stellar evolutionary models of SFD00, BHAC15 and F16 are consistent with the dynamical masses within the 1σ to 2σ uncertainties. On the contrary, magnetic F16 results in a deviation of 2.6σ . Compared to the dynamical measurement, magnetic F16 overestimates the stellar mass by $28^{+10}_{-11}\%$. C14 and PS99 result in deviations between 3σ to 4σ . Palla & Stahler (1999) underestimates the stellar mass by $21\pm 6\%$, while Chen et al. (2014) overestimates the stellar mass by $48^{+12}_{-13}\%$. Br12 shows the largest deviation of 5σ in this mass range, which underestimates the stellar masses by $30\pm 6\%$.

Table 9. Mean deviations between the spectroscopic and dynamical measurements in the respective mass ranges, including stars with $i > 70^\circ$

	0–0.6 M_\odot	0.6–1.3 M_\odot	1.3–3.0 M_\odot
Model	Deviation [%]	Deviation [%]	Deviation [%]
PS99	-21 ± 6	-27^{+6}_{-5}	-14^{+10}_{-8}
SFD00	-11 ± 7	-28^{+6}_{-5}	-9^{+10}_{-8}
Br12	-30 ± 6	-43 ± 5	-11^{+9}_{-7}
C14	48^{+12}_{-13}	-25^{+6}_{-5}	-11^{+9}_{-7}
BHAC15	-10 ± 8	-30 ± 6	-15^{+6}_{-5}
F16	-12^{+7}_{-8}	-34 ± 6	-11^{+9}_{-7}
magnetic F16	28^{+10}_{-11}	5^{+8}_{-7}	-15^{+8}_{-6}

NOTE—Negative values for the mean deviations where $M_{spec} < M_{dyn}$

Table 10. Mean deviations between the spectroscopic and dynamical measurements in the respective mass ranges, excluding stars with $i > 70^\circ$

	0–0.6 M_\odot	0.6–1.3 M_\odot	1.3–3.0 M_\odot
Model	Deviation [%]	Deviation [%]	Deviation [%]
PS99	-21 ± 6	-27^{+6}_{-5}	-11^{+14}_{-11}
SFD00	-11 ± 7	-28^{+6}_{-5}	-5^{+15}_{-12}
Br12	-30 ± 6	-43 ± 5	-7^{+14}_{-10}
C14	48^{+12}_{-13}	-25^{+6}_{-5}	-7^{+14}_{-10}
BHAC15	-10 ± 8	-30 ± 6	-14^{+10}_{-8}
F16	-12^{+7}_{-8}	-34 ± 6	-7^{+14}_{-11}
magnetic F16	28^{+10}_{-11}	5^{+8}_{-7}	-14^{+11}_{-8}

NOTE—Negative values for the mean deviations where $M_{spec} < M_{dyn}$

In the intermediate mass range, the magnetic F16 is the only model providing the stellar mass estimate consistent with the dynamical measurements within the 1σ uncertainty. All the other models included in the present paper result in spectroscopic masses deviating from the dynamical masses with mean deviations of more than 4σ . Compared to the dynamical measurement, these stellar evolutionary models underestimate the stellar mass by $\sim 20\%$ to $\sim 40\%$. In the high mass range, the spectroscopic masses estimated with the model of SFD00 best match the dynamical masses, with deviations of $\sim 1\sigma$ significance. Magnetic F16 and BHAC15 show deviations of 2σ to 3σ significance, while all other models show deviations between 1σ and 2σ . However,

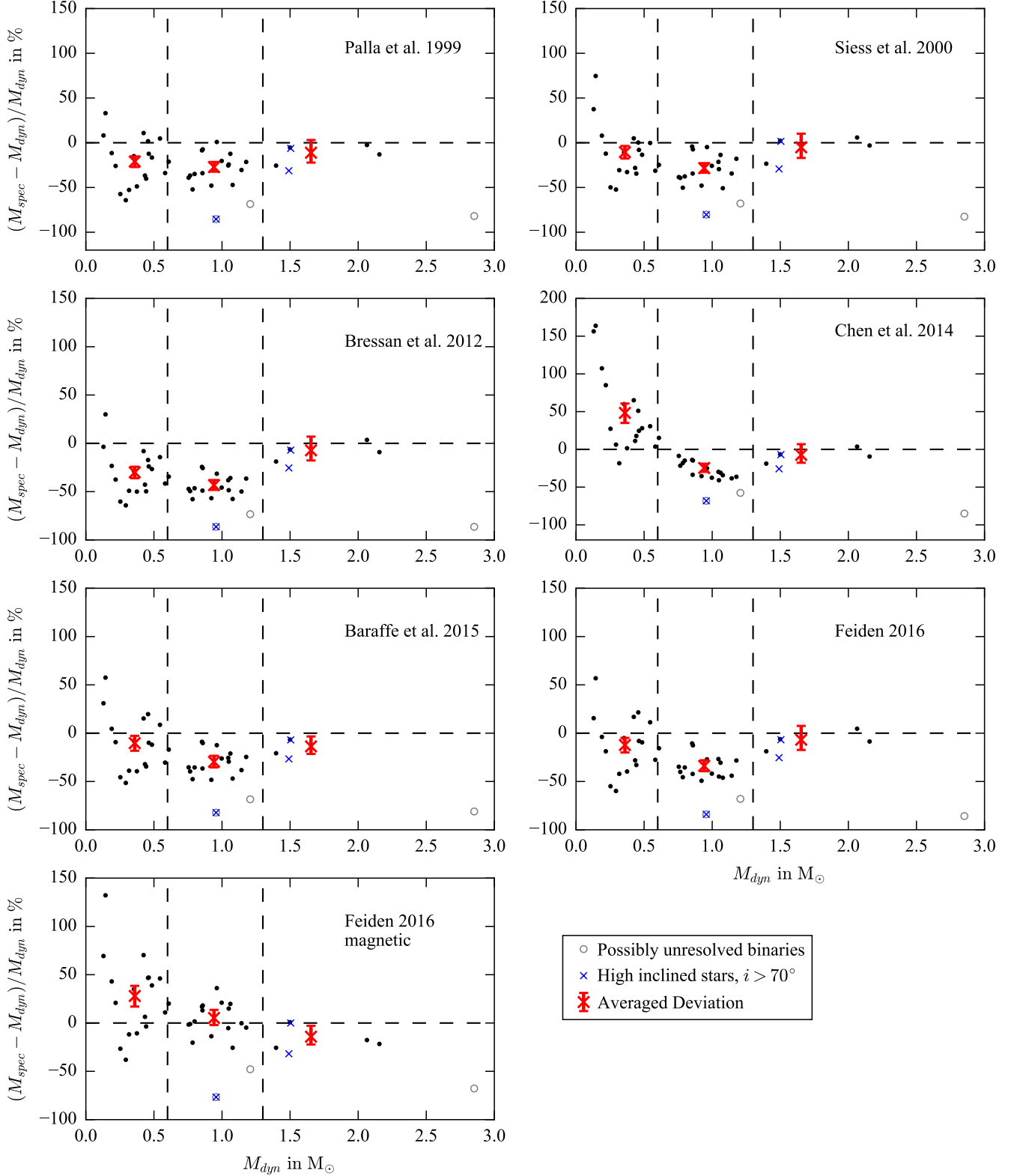


Figure 6. Deviation between the spectroscopic and dynamical stellar masses. The name of the model is labelled in the upper right corner of each diagram. Red crosses mark the mean deviations of the measurements in the respective mass ranges, and dashed vertical lines denote the three mass ranges. The calculated mean deviations are shown in Table 10. The stars, marked with grey circles, are candidates of unresolved binaries and are excluded from the comparisons. Stars marked with blue crosses are highly inclined sources ($i > 70^\circ$). The error bars for individual sources are not plotted here for clarity. The error bars range from 3% to 53% for all models except for the magnetic F16 and C14, for which the uncertainties go up to 80% and 108%, respectively. The shown uncertainties in the averaged deviations were calculated by propagating the uncertainties of the individual sources.

only six stars in our sample are in this mass range, and thus, the result of this mass range may not be fully reliable due to the small sample size.

We note that the mass of a star with a highly inclined disk can be overestimated with our analysis. The sources with an inclination angle $i > 70^\circ$ are marked by blue crosses in Figure 6. We also compared our dynamical measurement with the mass estimate from the stellar evolutionary models by excluding those sources. The results are shown in Table 10. The results in the low mass range do not change because there are no highly inclined sources in this mass range. The only high inclined star in the intermediate mass range, Sz84, is also a candidate for a possibly unresolved binary system, and is already excluded from our comparison. In the high mass range, the deviations between the spectroscopic and dynamical measurements decrease by about 20% to 40% and become smaller than 1σ for all models after the highly inclined sources are excluded, except for BHAC15 and the magnetic F16 model. However, our results of the high mass range are uncertain due to the small sample in this mass range.

In summary, our results show that the stellar evolutionary models of BHAC15, F16 and SFD00 are in good agreement ($1.4\sim 1.6\sigma$) with the dynamical measurements in the low mass range of $M_\star \leq 0.6 M_\odot$, while the other four models tend to under- or overestimate the stellar mass by 20% to 30%. In the intermediate mass range of $0.6 M_\odot \leq M_\star \leq 1.3 M_\odot$, our results suggest that all spectroscopic models systematically underestimate the stellar mass by 20% to 40%, except for the magnetic F16, which is in good agreement with the dynamical mass measurement with a deviation smaller than 0.7σ . In general, the agreement of the spectroscopic and dynamical measurement becomes better in the mass range of $M_\star \geq 1.3 M_\odot$, except for the magnetic F16. However, there are only a few sources in this mass range, and therefore we cannot make a reliable comparison.

6.3. Comparison with Literature

Hillenbrand & White (2004) assembled a data set consisting of 27 PMS stars and 88 MS stars, where the stellar masses were both spectroscopically and dynamically determined. The methods used to measure the dynamical stellar masses included eclipsing binary systems, astrometric and radial velocity orbits, disk kinematics and double-lined spectroscopic binaries. In their work, the spectroscopic masses were obtained using the evolutionary models of SFD00 and PS99, among others. The masses of the PMS stars included in their sample range from 0.3 to $1.9 M_\odot$, the masses of the MS stars

range from 0.1 to $2 M_\odot$. Four, ten, and eight PMS stars were included with masses below $0.5 M_\odot$, between $0.5 M_\odot$ and $1.2 M_\odot$, and above $1.2 M_\odot$, respectively. For PMS stars with masses above $1.2 M_\odot$ and in the range of 0.3 to $0.5 M_\odot$, all models were found to be in good agreement with the spectroscopic measurement with a mean deviation $< 1\sigma$. On the contrary, it was found that most evolutionary models underestimate stellar masses by $\sim 25\%$ in the range of $0.5 M_\odot$ to $1.2 M_\odot$ at $1\text{--}2\sigma$ significance. Thus, our results are consistent with the findings by Hillenbrand & White (2004) for the stellar evolutionary model of SFD00. In our results, a larger deviation was found for the evolutionary model of PS99 in the lowest mass range. However, this might be explained by the larger number of stars with masses smaller $0.5 M_\odot$, included in the present paper.

Simon et al. (2019) present the dynamical measurements of 29 stars from the Taurus and 3 in the Ophiuchus star-forming regions, using the rotation in the disks around the stars. The dynamical masses were compared to the spectroscopic masses from the non-magnetic evolutionary models by BHAC15 and F16, as well as the magnetic evolutionary model by Feiden (2016). The mass range of the sample in Simon et al. (2019) is from 0.4 to $1.4 M_\odot$. Simon et al. (2019) found that the non-magnetic evolutionary models underestimate the stellar mass by $\sim 30\%$ in this mass range. The magnetic F16 yields spectroscopic masses in good agreement with the dynamical measurements with deviations of only $0.01\pm 0.02 M_\odot$. Our results of the intermediate mass range also show the same tendency. To make a more detailed comparison, we separated the results in Simon et al. (2019) into the same mass ranges as those in Section 6.2 and calculated the mean deviations in the respective mass ranges. Three and seven stars were found in the low and intermediate mass range, respectively. For stars with masses $M_\star < 0.6 M_\odot$ deviations of $-14\pm 6\%$ for the non-magnetic and $21\pm 6\%$ for the magnetic model were found. For the intermediate mass stars ($0.6 M_\odot \leq M_\star \leq 1.3 M_\odot$) $-24\pm 3\%$ and $-4\pm 3\%$ were found, for the non-magnetic and the magnetic model, respectively. Thus, the trends in our results are consistent with those in Simon et al. (2019) for the same stellar evolutionary models.

Our results and those in the literature show the same tendency that most of the studied spectroscopic models tend to underestimate the masses of stars in the mass range of $0.4\text{--}0.6 M_\odot \lesssim M_\star \lesssim 1.2\text{--}1.4 M_\odot$ by 20%–40%, and only the magnetic F16 model provides an accurate mass estimate. Compared to the non-magnetic evolutionary models studied in the present paper, the magnetic F16 model suggests a factor of 2 older ages of a

star because of the slower contraction due to additional magnetic pressure. This could imply a longer T Tauri phase and thus longer time scales of star and planet formation (Simon et al. 2019; Feiden 2016). On the other hand, our results with a larger sample of low-mass stars than those in the literature further show that the stellar masses estimated with the magnetic F16 model are inconsistent with the dynamical masses for the low-mass stars with masses $\leq 0.6 M_{\odot}$ at a level of more than 2σ , while the stellar masses estimated with the other non-magnetic models by BHAC15, F16 and SFD00 are in a better agreement with the dynamical masses. Therefore, our study suggests that none of the stellar evolutionary models studied in the present paper can provide an accurate estimate of stellar mass over a wide mass range from $0.1 M_{\odot}$ to $1.4 M_{\odot}$. This result could hint at the mass dependence of physical processes which is possibly not accurately described in the stellar evolutionary models. Nevertheless, the accuracy of our dynamical mass measurements is limited by the S/N of the data. Higher S/N data and a larger sample covering a wide mass range from 0.1 to $1 M_{\odot}$ are needed to further reveal the mass dependence of the accuracy of the stellar evolutionary models.

7. SUMMARY

We analysed the ALMA archival data of ^{13}CO ($J = 2-1$ & $3-2$), C^{18}O ($J = 2-1$ & $3-2$), and CN ($N = 3-2$, $J = 7/2-5/2$) of 30 PMS stars in the Lupus star-forming region and of ^{13}CO ($J = 2-1$) and C^{18}O ($J = 2-1$) of 37 PMS stars in the Taurus star-forming region. For individual stars, we stacked the different molecular line data to enhance the S/Ns and measured the dynamical stellar masses from Keplerian rotation of their surrounding disks. The stellar masses were measured by maximizing the S/Ns by multiplying image cubes by various Keplerian rotational velocity patterns. After stacking different molecular lines, we obtained measurements of stellar masses for 45 out of 67 PMS stars with our method. We also obtained measurements when only using the data of individual lines, and the measured stellar masses from individual lines are consistent with each other within the uncertainties. In addition, we tested our method with synthetic ALMA images of chemical and physical disk models generated with the DALI code. Our method indeed can provide robust estimates of stellar mass. We compared the measured dynamical masses with the spectroscopically determined stellar masses with different stellar evolutionary models to examine the accuracy of these models.

For individual stars, most of our measured dynamical masses are consistent with the spectroscopic masses

within a 3σ level for all the stellar evolutionary models due to the limited S/Ns of our data. Given our sufficiently large sample, we separated our sample into three mass ranges and computed the mean differences between the dynamical and spectroscopic masses and the uncertainties of the mean differences in these mass ranges. Our results show that in the low mass range of $< 0.6 M_{\odot}$, the spectroscopic masses estimated with the stellar evolutionary models by Baraffe et al. (2015), Feiden (2016) (without magnetic field) and Siess et al. (2000) are in good agreement ($1.4\sim 1.6\sigma$) with the dynamical masses, while the other four models, Palla & Stahler (1999), Chen et al. (2014), Bressan et al. (2012), and Feiden (2016) (with magnetic field) tend to under- or overestimate the stellar mass by 20% to 30%. In the intermediate mass range of $0.6 M_{\odot} \leq M_{\star} \leq 1.3 M_{\odot}$, only the stellar evolutionary model with magnetic field by Feiden (2016) provides a stellar mass estimate in good agreement with the dynamical mass measurement ($< 0.7\sigma$). All the other models underestimate the stellar mass by 20% to 40% compared to the dynamical masses. After excluding the high-inclined sources, all models show deviations $< 1\sigma$ in the mass range of $\geq 1.3 M_{\odot}$, except for the model of Baraffe et al. (2015) and the magnetic Feiden (2016) including magnetic fields, which show deviations of 2σ . However, our sample only contains a few sources in this mass range, so we cannot make a fully reliable comparison for this mass range.

Therefore, our study suggests that none of the stellar evolutionary models studied in the present paper can provide an accurate estimate of stellar mass over a wide mass range from $0.1 M_{\odot}$ to $1.4 M_{\odot}$. This result could hint at the mass dependence of physical processes which is possibly not accurately described in the stellar evolutionary models.

ACKNOWLEDGMENTS

We thank Patrick D. Sheehan for his help and the discussions on the stellar mass estimate with the spectroscopic measurements using the stellar evolutionary models. This paper makes use of the following ALMA data: ADS/JAO.ALMA#2013.1.00220.S, ADS/JAO.ALMA#2015.1.00222.S, ADS/JAO.ALMA#2016.1.01239.S, ADS/JAO.ALMA#2016.1.01164.S. ALMA is a partnership of ESO (representing its member states), NSF (USA) and NINS (Japan), together with NRC (Canada), MOST and ASIAA (Taiwan), and KASI (Republic of Korea), in cooperation with the Republic of Chile. The Joint ALMA Observatory is operated by ESO, AUI/NRAO and NAOJ. This work has made use of data from the European Space Agency (ESA) mission *Gaia* (<https://www.cosmos.esa.int/gaia>), processed by the *Gaia* Data Processing and Analysis Consortium (DPAC, <https://www.cosmos.esa.int/web/gaia/dpac/consortium>). Funding for the DPAC has been provided by national institutions, in particular the institutions participating in the *Gaia* Multilateral Agreement. This project has received funding from the European Union’s Horizon 2020 research and innovation programme under the Marie Skłodowska-Curie grant agreement No 823823 (DUSTBUSTERS). This work was partly supported by the Deutsche Forschungsgemeinschaft (DFG, German Research Foundation) - Ref no. FOR 2634/1 TE 1024/1-1, by the Italian Ministero dell’Istruzione, Università e Ricerca (MIUR) through the grant Progetti Premiali 2012 iALMA (CUP C52I13000140001), and by the DFG cluster of excellence Origin and Structure of the Universe (www.universe-cluster.de). H.-W.Y. acknowledges support from MOST 108-2112-M-001-003-MY2. P.M.K. acknowledges support from MOST 108-2112-M-001-012 and MOST 109-2112-M-001-022, and from an Academia Sinica Career Development Award.

REFERENCES

- Alcalá, J., Manara, C., France, K., et al. 2019, *Astronomy & Astrophysics*, 629, A108
- Alcalá, J., Natta, A., Manara, C., et al. 2014, *Astronomy & Astrophysics*, 561, A2
- Alcalá, J., Manara, C., Natta, A., et al. 2017, *Astronomy & Astrophysics*, 600, A20
- Ansdell, M., Williams, J. P., Manara, C. F., et al. 2017, *The Astronomical Journal*, 153, 240
- Ansdell, M., Williams, J. P., van der Marel, N., et al. 2016, *The Astrophysical Journal*, 828, 46, doi: [10.3847/0004-637x/828/1/46](https://doi.org/10.3847/0004-637x/828/1/46)
- Ansdell, M., Williams, J. P., Trapman, L., et al. 2018, *The Astrophysical Journal*, 859, 21, doi: [10.3847/1538-4357/aab890](https://doi.org/10.3847/1538-4357/aab890)
- Baraffe, I., Chabrier, G., Allard, F., & Hauschildt, P. 1998, arXiv preprint astro-ph/9805009
- Baraffe, I., Chabrier, G., & Gallardo, J. 2009, *The Astrophysical Journal Letters*, 702, L27
- Baraffe, I., Homeier, D., Allard, F., & Chabrier, G. 2015, *Astronomy & Astrophysics*, 577, A42
- Barenfeld, S. A., Carpenter, J. M., Ricci, L., & Isella, A. 2016, *The Astrophysical Journal*, 827, 142

- Bressan, A., Marigo, P., Girardi, L., et al. 2012, *Monthly Notices of the Royal Astronomical Society*, 427, 127
- Bruderer, S. 2013, *Astronomy & Astrophysics*, 559, A46
- Bruderer, S., van Dishoeck, E. F., Doty, S. D., & Herczeg, G. J. 2012, *Astronomy & Astrophysics*, 541, A91
- Burkert, A. 2004, arXiv preprint astro-ph/0404015
- Cassisi, S. 2012, in *Red Giants as Probes of the Structure and Evolution of the Milky Way* (Springer), 57–68
- Cazzoletti, P., Manara, C., Liu, H. B., et al. 2019, *Astronomy & Astrophysics*, 626, A11
- Ceverino, D., & Klypin, A. 2009, *The Astrophysical Journal*, 695, 292
- Chen, Y., Girardi, L., Bressan, A., et al. 2014, *Monthly Notices of the Royal Astronomical Society*, 444, 2525
- D’Antona, F., & Mazzitelli, I. 1997, *Memorie della Societa Astronomica Italiana*, 68, 807
- Eisner, J. A., Arce, H., Ballering, N., et al. 2018, *The Astrophysical Journal*, 860, 77
- El-Badry, K., Rix, H.-W., Ting, Y.-S., et al. 2018, *Monthly Notices of the Royal Astronomical Society*, 473, 5043
- Feiden, G. A. 2016, *Astronomy & Astrophysics*, 593, A99
- Gaia Collaboration, Brown, A., Vallenari, A., Prusti, T., et al. 2018, *Astronomy & Astrophysics*, 616, A1
- Gaia Collaboration, Prusti, T., De Bruijne, J., Brown, A. G., et al. 2016, *Astronomy & Astrophysics*, 595, A1
- Guilloteau, S., Simon, M., Piétu, V., et al. 2014, *Astronomy & Astrophysics*, 567, A117
- Herczeg, G. J., & Hillenbrand, L. A. 2014, *The Astrophysical Journal*, 786, 97
- . 2015, *The Astrophysical Journal*, 808, 23
- Hillenbrand, L. A., & White, R. J. 2004, *The Astrophysical Journal*, 604, 741
- Hopkins, A. 2018, *Publications of the Astronomical Society of Australia*, 35
- Jeffries, R. 2012, *European Astronomical Society Publications Series*, 57, 45
- Long, F., Pinilla, P., Herczeg, G. J., et al. 2018, *The Astrophysical Journal*, 869, 17
- Long, F., Herczeg, G. J., Harsono, D., et al. 2019, *The Astrophysical Journal*, 882, 49
- Manara, C., Testi, L., Herczeg, G., et al. 2017, *Astronomy & Astrophysics*, 604, A127
- Manara, C., Tazzari, M., Long, F., et al. 2019, arXiv preprint arXiv:1907.03846
- Mathieu, R. D., Stassun, K., Basri, G., et al. 1997, *The Astronomical Journal*, 113, 1841
- Matrà, L., MacGregor, M. A., Kalas, P., et al. 2017, *The Astrophysical Journal*, 842, 9
- Miotello, A., van Dishoeck, E. F., Kama, M., & Bruderer, S. 2016, *Astronomy & Astrophysics*, 594, A85
- Palla, F., & Stahler, S. W. 1993, *The Astrophysical Journal*, 418, 414
- . 1999, *The Astrophysical Journal*, 525, 772
- Pinte, C., Ménard, F., Duchêne, G., et al. 2018, *Astronomy & Astrophysics*, 609, A47
- Prato, L., Simon, M., Mazeh, T., Zucker, S., & McLean, I. 2002, *The Astrophysical Journal Letters*, 579, L99
- Rigliaco, E., Natta, A., Testi, L., et al. 2012, *Astronomy & Astrophysics*, 548, A56
- Rizzuto, A. C., Dupuy, T. J., Ireland, M. J., & Kraus, A. L. 2019, arXiv preprint arXiv:1911.12378
- Rizzuto, A. C., Ireland, M. J., Dupuy, T. J., & Kraus, A. L. 2016, *The Astrophysical Journal*, 817, 164
- Salinas, V., Hogerheijde, M., Mathews, G., et al. 2017, *Astronomy & Astrophysics*, 606, A125
- Sheehan, P. D., Wu, Y.-L., Eisner, J. A., & Tobin, J. J. 2019, *The Astrophysical Journal*, 874, 136
- Siess, L., Dufour, E., & Forestini, M. 2000, arXiv preprint astro-ph/0003477
- Simon, M., Dutrey, A., & Guilloteau, S. 2000, *The Astrophysical Journal*, 545, 1034
- Simon, M., Guilloteau, S., Di Folco, E., et al. 2017, *The Astrophysical Journal*, 844, 158
- Simon, M., Guilloteau, S., Beck, T. L., et al. 2019, *The Astrophysical Journal*, 884, 42
- Stassun, K. G., Feiden, G. A., & Torres, G. 2014, *New Astronomy Reviews*, 60, 1
- Tazzari, M., Testi, L., Natta, A., et al. 2017, *Astronomy and Astrophysics*, 606, A88, doi: [10.1051/0004-6361/201730890](https://doi.org/10.1051/0004-6361/201730890)
- Teague, R., Bae, J., Bergin, E. A., Birnstiel, T., & Foreman-Mackey, D. 2018a, *The Astrophysical Journal Letters*, 860, L12
- Teague, R., Henning, T., Guilloteau, S., et al. 2018b, *The Astrophysical Journal*, 864, 133
- Trapman, L., Ansdell, M., Hogerheijde, M., et al. 2020, arXiv preprint arXiv:2004.07257
- van Terwisga, S., van Dishoeck, E., Ansdell, M., et al. 2018, arXiv preprint arXiv:1805.03221
- van Terwisga, S. E., van Dishoeck, E. F., Mann, R. K., et al. 2020, arXiv preprint arXiv:2004.13551
- Williams, J. P., Cieza, L., Hales, A., et al. 2019, *The Astrophysical Journal Letters*, 875, L9
- Yen, H.-W., Koch, P. M., Liu, H. B., et al. 2016, *The Astrophysical Journal*, 832, 204, doi: [10.3847/0004-637X/832/2/204](https://doi.org/10.3847/0004-637X/832/2/204)
- Yen, H.-W., Koch, P. M., Manara, C. F., Miotello, A., & Testi, L. 2018, *Astronomy and Astrophysics*, 616, A100, doi: [10.1051/0004-6361/201732196](https://doi.org/10.1051/0004-6361/201732196)

APPENDIX

A. DISTRIBUTION OF THE STELLAR PARAMETERS

Histograms of the luminosity, effective temperature and stellar mass are shown in Figure 7, to give an overview over the distribution of the parameters of the stars included in this paper.

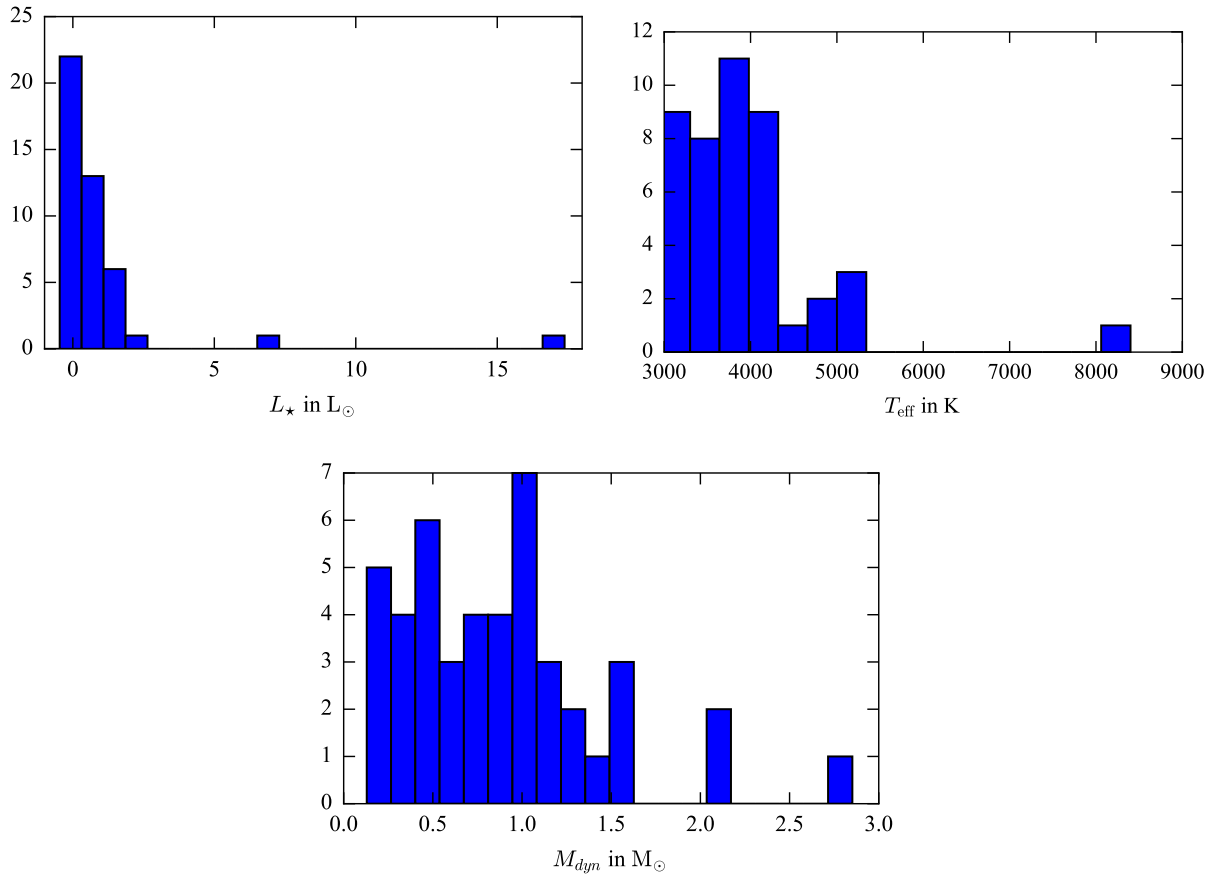


Figure 7. Distribution of the luminosity (L_*), effective temperature (T_{eff}), and dynamical stellar mass (M_{dyn}) of the stars included in this paper

B. ALIGNED SPECTRA FOR THE SOURCES IN THE LUPUS AND TAURUS STAR-FORMING REGIONS

Figures 8 and 9 show the original, non-aligned (black) and the aligned (red) spectra of the sources in the Lupus and Taurus star-forming regions, respectively. These spectra are extracted from the combination of the molecular-line data which results in the highest S/N (Section 4), and these are the spectra adopted to obtain the final measurements.

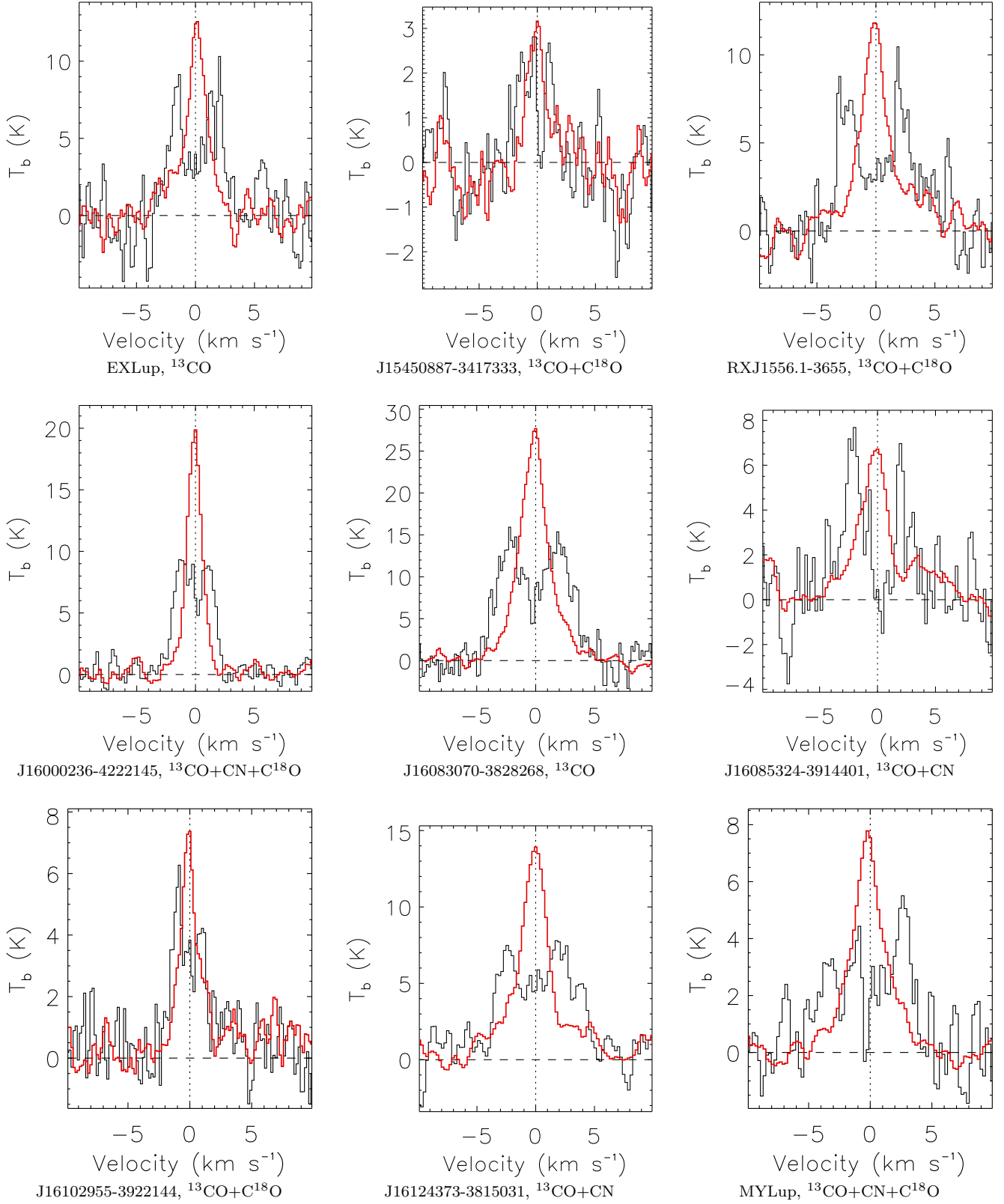


Figure 8. Original (black histograms) and velocity aligned (red histograms) spectra for the sources in the Lupus star-forming region

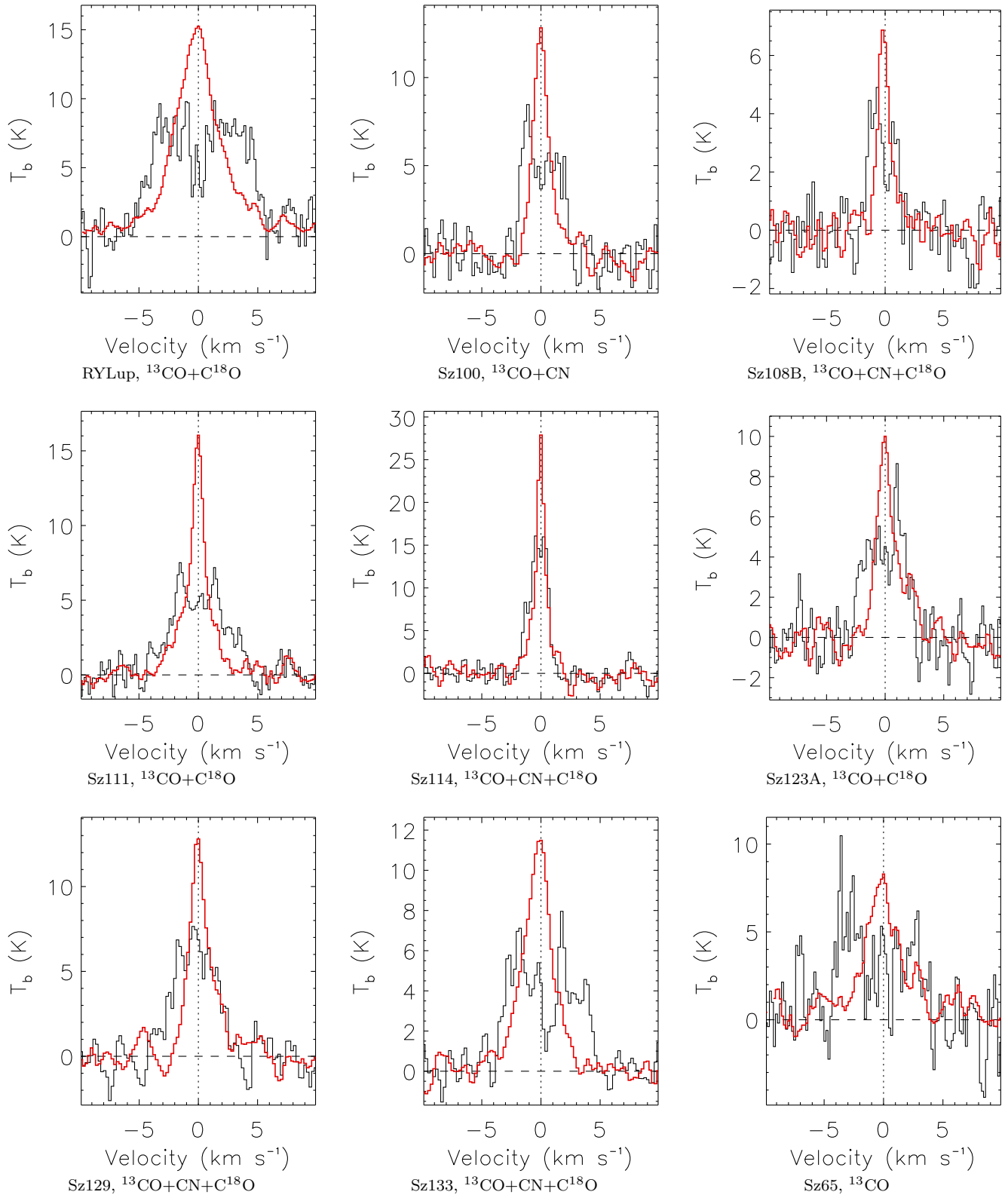


Figure 8 continued

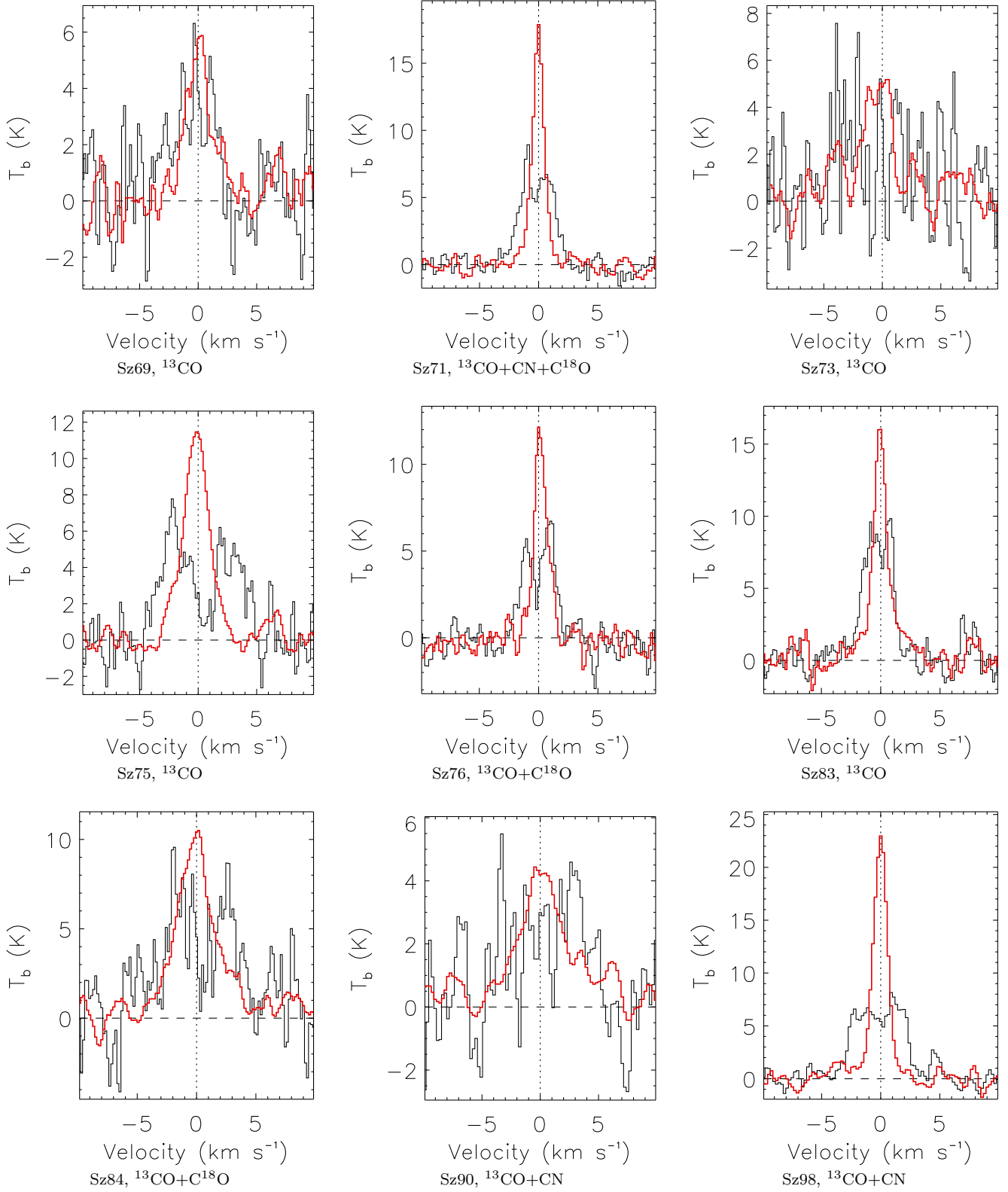


Figure 8 continued

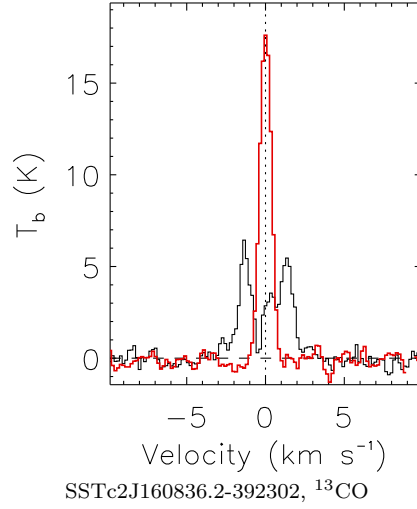


Figure 8 continued

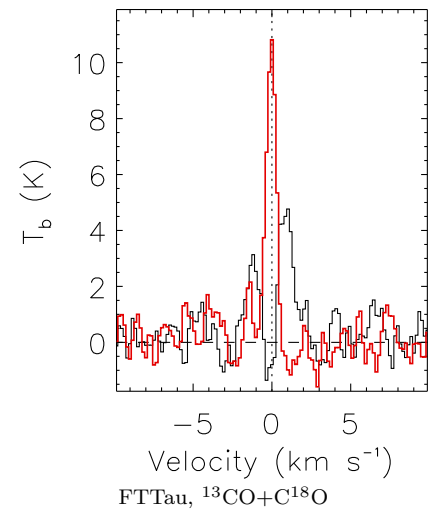
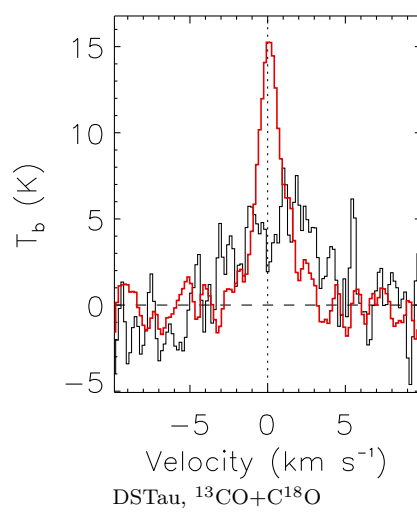
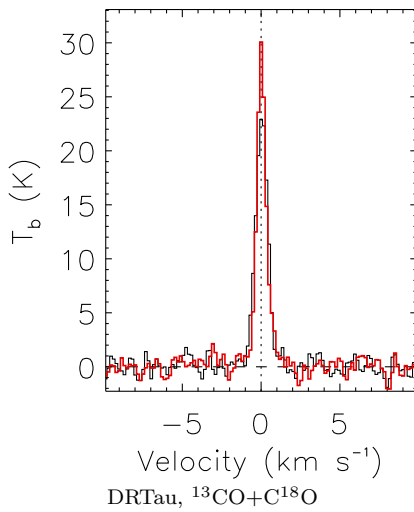
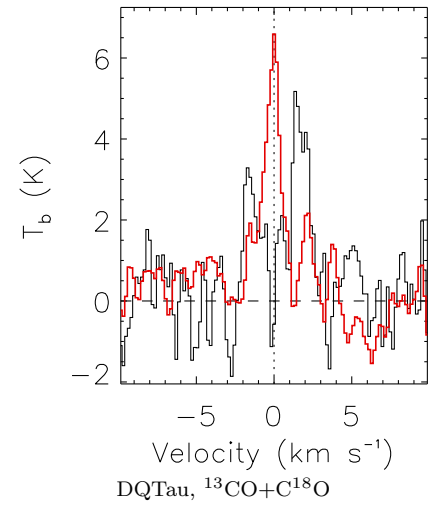
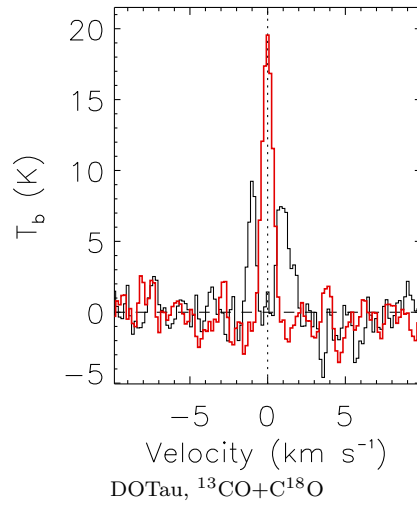
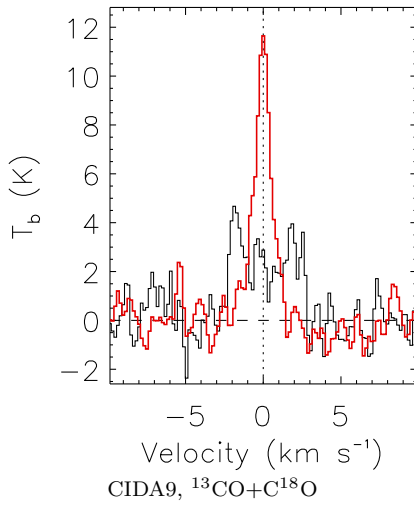


Figure 9. Original (black histograms) and velocity aligned (red histograms) spectra for the sources in the Taurus star-forming region

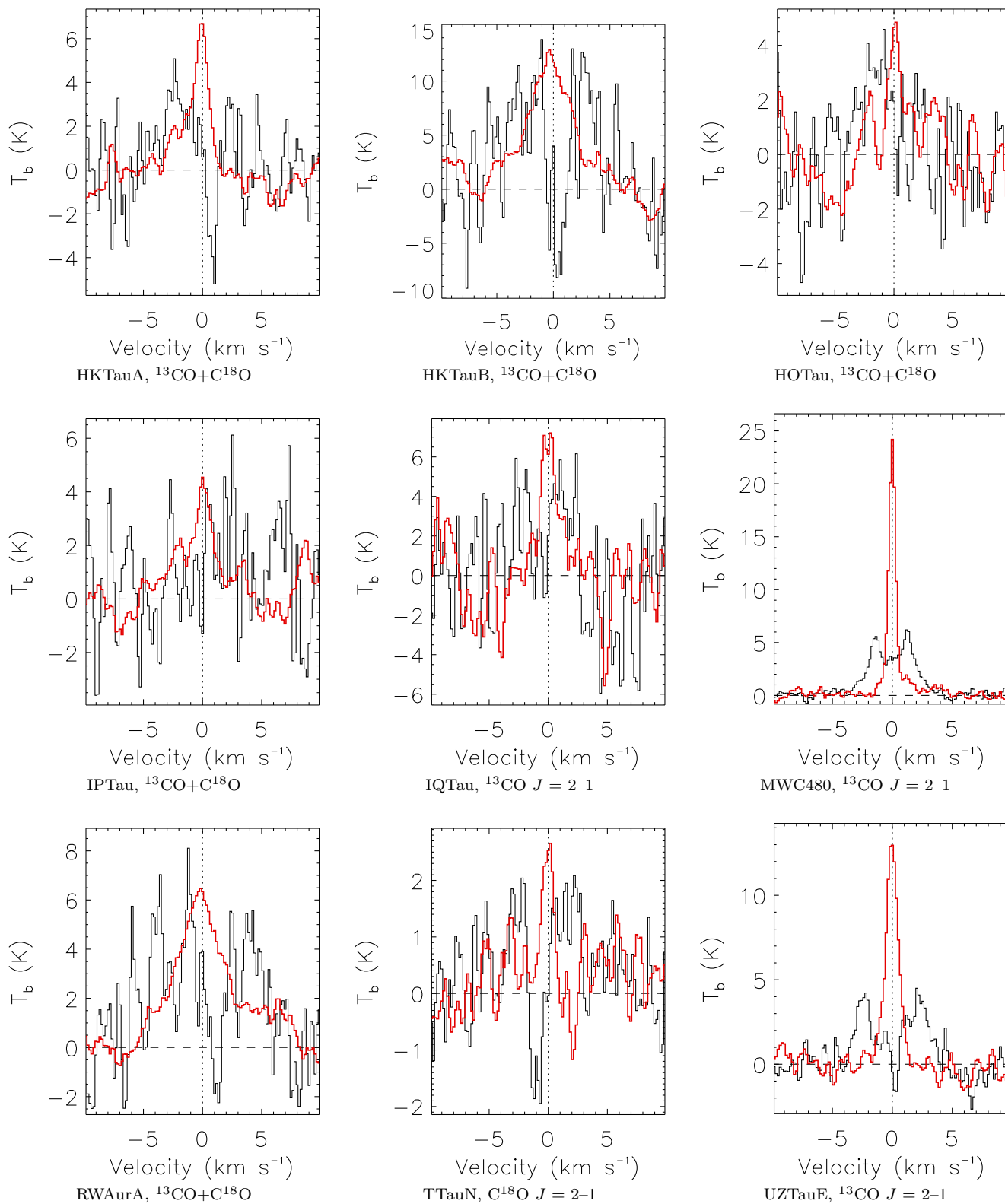


Figure 9 continued

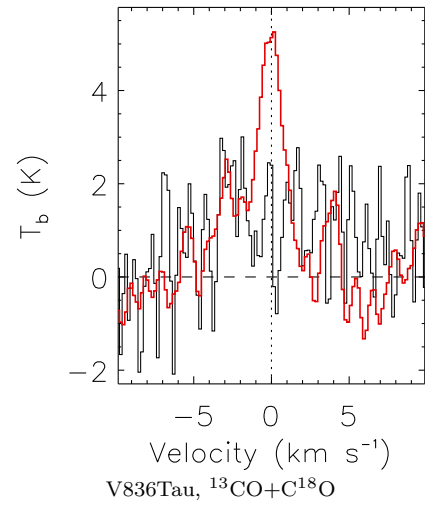
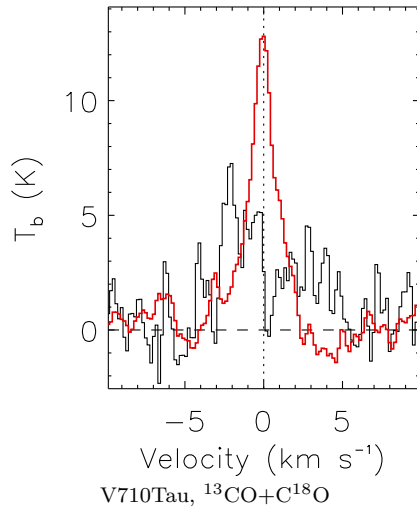


Figure 9 continued

C. TESTING THE ANALYSIS ON SYNTHETIC DATA

Figure 10 presents an example of the tests on our analysis using the synthetic ^{13}CO (3–2) data. In this example, the synthetic data were generated from our model disk with an inclination angle 45° , a position angle of 90° , a scale height of $h/R = 0.2$, a disk mass of $0.001 M_\odot$, and a stellar mass of $1.1 M_\odot$ using the CASA simulator. The uv-coverage in the imaging simulations was adopted to be similar to that of the Band 7 data of the Lupus YSOs. Figure 10a shows the synthetic spectra without noise. The black histograms show the original spectrum directly extracted from the synthetic data cube, and the spectrum exhibits double peaks due to the Doppler shifted emission in the disk. The red histograms show the spectrum after the velocity alignment with the model parameters described above. After the velocity alignment, the spectrum becomes single-peaked because the Doppler shift due to the disk rotation is all corrected to zero velocity. Figure 10b shows the same synthetic data but with the noise included in the imaging simulations. The noise level was adopted to be similar to that in our real data. The double peak is less visible because of the relatively low S/N. Then we applied our analysis described in Section 4 to measure the stellar mass from the synthetic data. After applying our analysis, the spectrum (red histograms) is properly aligned to have a clear single peak. The stellar mass is measured to be $1.1^{+0.1}_{-0.05} M_\odot$ consistent with the model input within 1σ . This example demonstrates that our method indeed gives the expected result.

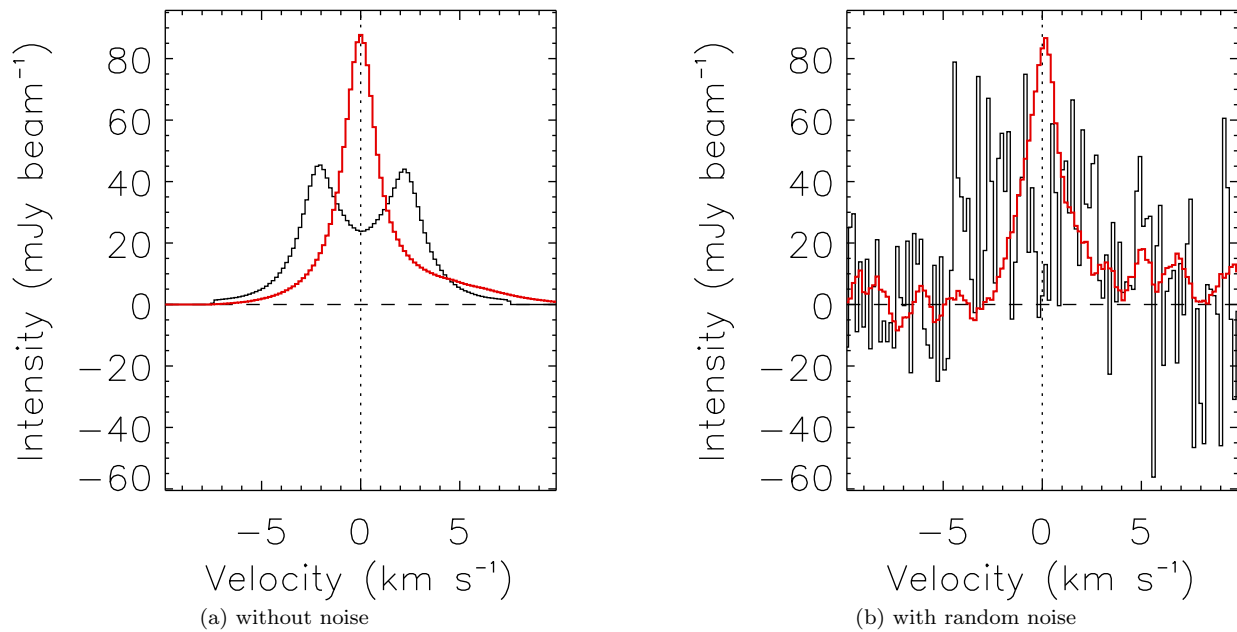


Figure 10. Original (black histogram) and velocity aligned (red histograms) spectra for synthesised data.

D. SPECTROSCOPIC MASSES

All values for the spectroscopic masses calculated by using the evolutionary models of Palla & Stahler (1999), Siess et al. (2000), Bressan et al. (2012), Chen et al. (2014), Baraffe et al. (2015) and Feiden (2016) are given in Table 11 and Table 12 for the sources in the Lupus and Taurus star-forming region, respectively.

Table 11. Spectroscopic masses of different evolutionary models for the sources in the Lupus star-forming region

Name	PS99 [M_{\odot}]	SFD00 [M_{\odot}]	Br12 [M_{\odot}]	C14 [M_{\odot}]	BHAC15 [M_{\odot}]	F16 [M_{\odot}]	magnetic F16 [M_{\odot}]
Sz65	0.80 ± 0.12	0.75 ± 0.11	0.57 ± 0.15	0.70 ± 0.12	0.71 ± 0.17	0.64 ± 0.16	1.14 ± 0.13
J15450887-3417333	0.108 ± 0.016	0.127 ± 0.019	0.101 ± 0.010	0.32 ± 0.05	0.14 ± 0.03	0.114 ± 0.025	0.19 ± 0.04
Sz68	2.1 ± 0.3	2.2 ± 0.3	1.6 ± 0.4	1.6 ± 0.4	1.40 ± 0.03	1.6 ± 0.4	1.68 ± 0.22
Sz69	0.162 ± 0.024	0.192 ± 0.029	0.137 ± 0.025	0.40 ± 0.06	0.20 ± 0.04	0.18 ± 0.04	0.26 ± 0.06
Sz71	0.41 ± 0.06	0.43 ± 0.06	0.35 ± 0.09	0.58 ± 0.13	0.42 ± 0.11	0.42 ± 0.11	0.68 ± 0.15
Sz73	0.80 ± 0.12	0.80 ± 0.12	0.64 ± 0.1	0.73 ± 0.09	0.77 ± 0.16	0.75 ± 0.16	1.01 ± 0.10
Sz75	0.97 ± 0.15	0.92 ± 0.14	0.66 ± 0.18	0.72 ± 0.15	0.84 ± 0.18	0.70 ± 0.18	1.31 ± 0.17
Sz76	0.192 ± 0.029	0.25 ± 0.04	0.19 ± 0.03	0.38 ± 0.08	0.23 ± 0.04	0.23 ± 0.04	0.34 ± 0.07
RXJ1556.1-3655	0.46 ± 0.07	0.47 ± 0.07	0.40 ± 0.11	0.69 ± 0.10	0.49 ± 0.13	0.49 ± 0.13	0.74 ± 0.14
Sz82	1.19 ± 0.18	1.13 ± 0.17	0.77 ± 0.21	0.77 ± 0.20	1.06 ± 0.18	0.79 ± 0.21	1.4 ± 0.3
Sz83	0.80 ± 0.12	0.74 ± 0.11	0.54 ± 0.14	0.62 ± 0.13	0.74 ± 0.15	0.58 ± 0.14	1.21 ± 0.23
Sz84	0.140 ± 0.021	0.188 ± 0.028	0.130 ± 0.022	0.30 ± 0.08	0.170 ± 0.028	0.15 ± 0.03	0.22 ± 0.07
Sz129	0.78 ± 0.12	0.82 ± 0.12	0.64 ± 0.16	0.73 ± 0.09	0.78 ± 0.15	0.76 ± 0.15	1.00 ± 0.10
RYLup	1.42 ± 0.21	1.53 ± 0.23	1.40 ± 0.18	1.40 ± 0.18	1.40 ± 0.08	1.41 ± 0.17	1.51 ± 0.13
J16000236-4222145	0.192 ± 0.029	0.25 ± 0.04	0.19 ± 0.03	0.38 ± 0.08	0.23 ± 0.04	0.23 ± 0.04	0.33 ± 0.07
MYLup	1.03 ± 0.15	1.06 ± 0.16	1.11 ± 0.11	1.11 ± 0.10	1.09 ± 0.11	1.11 ± 0.11	1.02 ± 0.10
EXLup	0.57 ± 0.08	0.56 ± 0.08	0.44 ± 0.11	0.57 ± 0.13	0.54 ± 0.13	0.50 ± 0.13	0.97 ± 0.16
Sz90	0.78 ± 0.12	0.82 ± 0.12	0.65 ± 0.15	0.73 ± 0.08	0.78 ± 0.15	0.77 ± 0.15	0.99 ± 0.09
Sz91	0.49 ± 0.07	0.46 ± 0.07	0.40 ± 0.11	0.70 ± 0.08	0.51 ± 0.13	0.52 ± 0.13	0.73 ± 0.12
Sz98	0.80 ± 0.12	0.74 ± 0.11	0.54 ± 0.14	0.62 ± 0.13	0.74 ± 0.15	0.58 ± 0.14	1.21 ± 0.23
Sz100	0.105 ± 0.016	0.140 ± 0.021	0.105 ± 0.013	0.31 ± 0.06	0.142 ± 0.028	0.118 ± 0.026	0.18 ± 0.04
J16083070-3828268	1.41 ± 0.21	1.53 ± 0.23	1.40 ± 0.18	1.40 ± 0.18	1.40 ± 0.08	1.40 ± 0.17	1.50 ± 0.13
SST:c2dJ160836.2-392302	0.93 ± 0.14	0.92 ± 0.14	0.68 ± 0.18	0.73 ± 0.15	0.84 ± 0.19	0.74 ± 0.18	1.27 ± 0.12
Sz108B	0.140 ± 0.021	0.178 ± 0.027	0.125 ± 0.021	0.33 ± 0.07	0.169 ± 0.030	0.15 ± 0.03	0.22 ± 0.06
J16085324-3914401	0.28 ± 0.04	0.31 ± 0.05	0.25 ± 0.04	0.48 ± 0.09	0.29 ± 0.05	0.31 ± 0.05	0.46 ± 0.08
Sz111	0.48 ± 0.07	0.46 ± 0.07	0.40 ± 0.11	0.70 ± 0.08	0.51 ± 0.13	0.51 ± 0.13	0.73 ± 0.12
Sz114	0.150 ± 0.023	0.22 ± 0.03	0.161 ± 0.026	0.26 ± 0.07	0.194 ± 0.027	0.18 ± 0.03	0.28 ± 0.07
J16102955-3922144	0.168 ± 0.025	0.21 ± 0.03	0.146 ± 0.026	0.39 ± 0.07	0.20 ± 0.04	0.18 ± 0.04	0.27 ± 0.06
Sz123A	0.47 ± 0.07	0.46 ± 0.07	0.38 ± 0.10	0.69 ± 0.05	0.55 ± 0.12	0.56 ± 0.12	0.67 ± 0.10
J16124373-3815031	0.49 ± 0.07	0.47 ± 0.07	0.39 ± 0.10	0.60 ± 0.12	0.46 ± 0.12	0.46 ± 0.12	0.76 ± 0.15

NOTE—(PS99) Palla & Stahler (1999); (SFD00) Stess et al. (2000); (Br12) Bressan et al. (2012); (C14) Chen et al. (2014); (BHAC15) Baraffe et al. (2015); (F16) Feiden (2016)

NOTE—We were not able to obtain reliable spectroscopic masses for Sz133, because the location of this source in the HR diagram does not overlap with the evolutionary models of PMS stars. Thus, Sz133 was excluded from the comparison.

Table 12. Spectroscopic masses of different evolutionary models for the sources in the Taurus star-forming region

Name	PS99 [M_{\odot}]	SFD00 [M_{\odot}]	Br12 [M_{\odot}]	C14 [M_{\odot}]	BHAC15 [M_{\odot}]	F16 [M_{\odot}]	magnetic F16 [M_{\odot}]
CIDA9A	0.38±0.06	0.39±0.06	0.33±0.09	0.64±0.11	0.41±0.12	0.43±0.12	0.62±0.14
DOTau	0.57±0.09	0.54±0.08	0.47±0.12	0.71±0.06	0.59±0.14	0.61±0.14	0.80±0.11
DQTau	0.52±0.08	0.50±0.07	0.39±0.10	0.43±0.11	0.54±0.10	0.41±0.10	0.92±0.26
DRTau	0.93±0.14	0.97±0.15	0.75±0.18	0.75±0.13	0.89±0.17	0.84±0.17	1.12±0.10
DSTau	0.57±0.09	0.53±0.08	0.46±0.12	0.71±0.07	0.57±0.14	0.58±0.14	0.80±0.12
FTTau	0.30±0.05	0.32±0.05	0.25±0.04	0.56±0.08	0.32±0.06	0.33±0.06	0.48±0.08
HKTauA	0.41±0.06	0.42±0.06	0.36±0.09	0.62±0.12	0.43±0.12	0.44±0.12	0.67±0.15
HOTau	0.27±0.04	0.29±0.04	0.22±0.04	0.52±0.08	0.29±0.05	0.30±0.06	0.43±0.08
IQTau	0.47±0.07	0.45±0.07	0.39±0.10	0.70±0.09	0.49±0.13	0.50±0.13	0.72±0.13
IPTau	0.52±0.08	0.50±0.07	0.43±0.11	0.68±0.10	0.52±0.14	0.52±0.14	0.81±0.14
MWC480	1.88±0.28	2.1±0.3	1.96±0.10	1.95±0.10	...	1.97±0.10	1.689±0.023
RWAurA	1.04±0.16	1.07±0.16	1.13±0.11	1.13±0.11	1.11±0.11	1.13±0.12	1.04±0.10
TTauN	2.0±0.3	2.2±0.3	2.14±0.26	2.14±0.26	...	2.16±0.27	1.70±0.07
UZTauE	0.38±0.06	0.39±0.06	0.32±0.08	0.51±0.13	0.38±0.10	0.39±0.10	0.63±0.15
V710Tau	0.39±0.06	0.40±0.06	0.34±0.09	0.60±0.12	0.40±0.12	0.42±0.12	0.65±0.15
V836Tau	0.48±0.07	0.48±0.07	0.40±0.10	0.60±0.12	0.48±0.13	0.47±0.12	0.80±0.15

NOTE—(PS99) Palla & Stahler (1999); (SFD00) Siess et al. (2000); (Br12) Bressan et al. (2012); (C14) Chen et al. (2014); (BHAC15) Baraffe et al. (2015); (F16) Feiden (2016)